NON-DISPERSIVE INFRARED (NDIR) GAS SENSORS UTILIZING LIGHT-EMITTING-DIODES SUITABLE FOR APPLICATIONS DEMANDING LOW-POWER AND LIGHTWEIGHT INSTRUMENTS

by

KYLE D. THURMOND
B.S. University of Central Florida, 2013

A thesis submitted in partial fulfillment of the requirements
for the degree of Master of Science
in the Department of Mechanical and Aerospace Engineering
in the College of Engineering and Computer Science
at the University of Central Florida
Orlando, Florida

Spring Term
2016

Major Professor: Subith S. Vasu

ABSTRACT

Gas sensors that are low-power, light-weight, and rugged, while also remaining low-cost, have considerable appeal to areas from automotive to space flight. There are increasing demands for higher efficient vehicles with lower emissions in order meet regulations that are meant to mitigate or lessen the effects of climate change. An affordable, fast response sensor that can measure transient carbon monoxide (CO) and carbon dioxide (CO_2) has broad application which can lead to more efficient, fuel flexible engines and regulations of harmful emissions. With compact, economical, low-power sensors that are able to continually monitor gases that are characteristic of burning materials, a distributed sensor array could be implemented on space vehicles that would allow early detection of fires, gas leaks, or other critical events. With careful selection of targeted gases, it may be possible to identify the material that is burning or smoldering, better informing the crew so that they may respond and prioritize high emergency events. Further applications may include fuel/ hazardous gas leak detection on space vehicles and atmospheric constituent sensor for portable life support systems (PLSS) used by astronauts in extra vehicular activity (EVA). Non-dispersive infrared (NDIR) sensors are attractive due to their simplicity and low-cost; and by using light-emitting-diodes (LEDs) in this approach, power efficient, light-weight, and stable gas sensors can be developed to meet these needs.

This thesis discusses a sensor that was developed for simultaneous, time resolved measurements of carbon monoxide (CO) and carbon dioxide (CO_2). This sensor utilizes low-cost and compact light emitting diodes (LEDs) that emit in the 3-5μm wavelength range. Light emission of LEDs is spectrally broader and more spatially divergent compared to that of lasers, which presented many design challenges. Optical design studies addressed some of the non-ideal

characteristics of the LED emissions. Measurements of CO and CO_2 were conducted using their fundamental absorption bands centered at 4.7μm and 4.3μm, respectively, while a 3.6μm reference LED was used to account for scattering losses (e.g., due to soot, window deposits, etc.) common to the three measurement LEDs. Instrument validation and calibration was performed using a laboratory flow cell and bottled-gas mixtures. The sensor was able to detect CO_2 and CO concentration changes as small as 30 ppm and 400 ppm, respectively. Because of the many control and monitor species with infra-red absorption features, which can be measured using the strategy described, this work demonstrates proof of concept for a wider range of fast (250Hz) and low cost sensors for gas measurement and process monitoring.

To my loving wife, Stephi, who inspires and fulfills me.

ACKNOWLEDGMENTS

I would like to express the gratitude I have for my advisor, Dr. Vasu, for his years of support, encouragement, and sharing his knowledge and experience with me. He has made this study possible and made many great opportunities available for me. I would also like to thank my committee members, Dr. Kassab and Dr. Kapat.

I must also thank my lab mates who have directly helped worked with on this project: Zachary Loparo, Justin Urso, and Michael Villar. Without their support this work certainly would not have progressed as far as it has or not have been quality of work as it is. At the very least, they have made the work a greater pleasure. I would also like to thank my lab mates that may have not directly worked with me on the project but certainly have contributed to my experience and knowledge along the way. Batikan Koroglu, Ghazal Barari, Joseph Lopez, Owen Prior, and Bader Almansour have been mentors and friends.

These people will be with me always.

TABLE OF CONTENTS

LIST OF FIGURES

LIST OF TABLES

CHAPTER 1: INTRODUCTION

Motivation

There is a crucial need to reduce the amount of fossils fuels used in order to mitigate dependencies on foreign oil, the effects of global climate change, and risks to public health. However, liquid fuel consumption is projected to increase by 38% from 2010 to 2040 with the transportation sector accounting for 63% of that increase [1]. There is not a single solution to these far-reaching issues and part of an overall solution will be moving from fossil fuels to biologically based liquid fuels that can have net zero carbon cycle while simultaneously improving combustion efficacies [2]. The development of sensors that are capable of detecting exhaust gases can assist in the advancement of adaptive engines that are fuel flexible with increased efficiency.

A sensor that can simultaneously monitor Carbon Monoxide (CO) and Carbon Dioxide (CO_2) will have benefits in emissions control and combustion control applications. CO is a primary product of incomplete combustion which can be used to indicate combustion efficiency. CO is also toxic to humans and animals, so is regulated by the U.S. Environmental Protection Agency. Regulations require Continues Emissions Monitory (CEM) in stationary sources that emit, or have the potential to emit, CO, including hazardous waste incinerators, boilers, and furnaces. CO_2 represents complete combustion, is a critical greenhouse gas, and, along with CO, is a measure of total exhaust carbon output. Greenhouse gases (GHG) increase the global average temperature by absorbing and emitting thermal radiation that would have otherwise escaped earth's atmosphere. The Intergovernmental Panel on Climate Change (IPCC) fifth assessment on climate change, released 2013, strengthened their degree of certainty that human activities are responsible for global climate change, reporting that is "extremely likely" (95 to 100% probability) [3]. The

changes are resulting in atmosphere and ocean warming, diminished snow and ice, higher and higher sea levels. Additionally, the total carbon output measure can be used to determine fuel input or in monitoring for future carbon regulations.

A sensor that can detect CO_2 in real-time can be used for Exhaust Gas Recirculation (EGR) monitoring and control. This is a well-established technique in reducing nitrogen oxides (NOx) formed at high temperatures in combustion engines. External EGR works by recirculating a portion of the exhaust gases back into the engine. Whereas in internal EGR the residual burned gas remains in the cylinder from the previous cycle, which makes it more difficult monitor. The effect of this technique is a reduction in flame temperatures by increasing the heat capacity of the inlet charge without altering the air to fuel ratio which can also benefit fuel economy. Poor EGR control can result in excessive quenching of the mixture leading to poor combustion quality and may increase difficulties to burn smoke free [4].

A series of gas sensors that are low-power and lightweight have a variety of applications in space flight which are specifically cited in NASA's 2015 Technology Roadmaps [5]. Under Technology Area 6: Human Health, Life Support, and Habitation Systems, they describe two applications in that this technology would be suitable which include an atmospheric constituent sensor for portable life support systems (PLSS) used in extra vehicular activity (EVA) [TA6.2.2.9] and fire detection systems [TA6.4.2.2].

NASA's Space Technology Roadmaps, topic 6.2.2.9 describes the need for an in-suit atmospheric constituent sensor for PLSS which will need to be small volume, be able to reject heat in various environments (i.e. Martian), has a low sampling rate, is accurate in 3 to 23psia range,

and is not susceptible to humidity. The key gases to be targeted by this sensor are those related to metabolic functions such as ammonia (NH_3), carbon dioxide (CO_2), water vapor H_2O, and oxygen (O_2). The sensor that is discussed here already detects CO_2 with a sensitivity of 30ppm (1atm) and can be extended to measure NH_3 and H_2O. Figure 1 suggests that CO_2 detection sensitivity to humidity should be minimal however with H_2O measurements, calibrations can be used to reduce noise. Thermal control of the sensing head may mitigate free water formation from interfering at the measuring site.

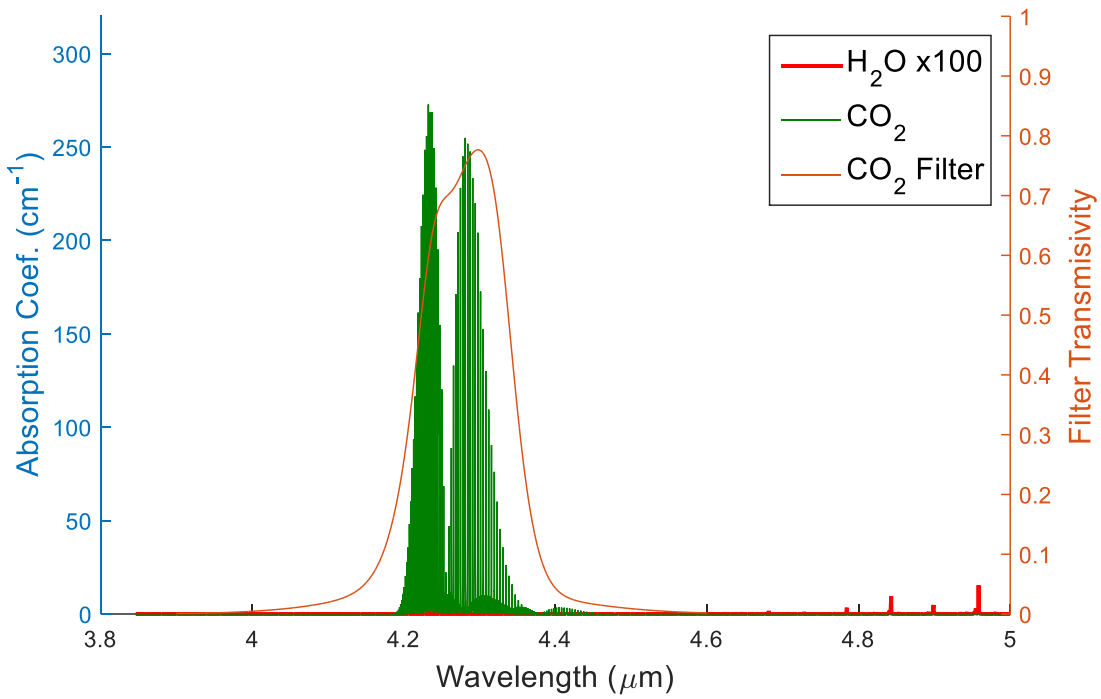

Figure 1: CO_2 absorption spectrum, water absorption spectrum (x100 for visibility), and the CO_2 bandpass filter. Water features negligible in this region. Features calculated at 4psia.

Topic 6.4.2 on NASA's Technology Roadmap states that fire detection and suppression is of paramount importance [5]. The proposed detection system aims to accomplish the goal of improving the threshold for detecting a fire, as well as eliminating false positives. Current sensors

used to detect fires use forward scattering near-inferred lasers to identify particles characteristic of smoke. However, non-combustion particles can interfere with the system, causing a false positive. On manned missions into deep space, waste will accumulate in the vessel, leading to an increased chance of a false alarm. It is suggested that a more robust approach would be to combine the smoke particle detection method with gaseous combustion byproducts such as CO_2, CO, etc. Subheading 6.4.2.2 of the STR specifically demonstrates an interest in fire detection in manned space vehicles [5]. The technology discussed here can be used for developing affordable distributed sensors sensitive to targeted combustion byproducts. Using LEDs instead of lasers, significantly reducing the power consumption of the detection system, are compact allowing placement in out of the way/targeted locations such as wire panels, and the low cost would allow high redundancy in the occurrence a sensor fails.

It is my opinion, and that of the Center of Excellence Commercial Space Transportation (FAA COE CST), that fire detection systems should be extended beyond the crew cabin to areas that may be kept at lower pressures. Such occurrence may include cargo bays, fuel/oxidizer tank storage, transitions from partially-closed life support systems to a more fully-closed integrated system, etc. It is therefore desirable to have sensors that can operate in the wide range of environments that are encountered in space missions and, furthermore, be able to detect a variety of gaseous species such as CO and CO_2 (indicators of fire and metabolic byproduct), NH_3, hydrocarbons (fuel leaks), N_2O (oxidizer), and H_2O. It is for this reason that environmental chamber tests were conducted for validation of this technology for future applications as a space vehicle fire and hazard detection sensor. Furthermore, high altitude balloon flights have been secured and sensor is currently undergoing preparations for further validation measures.

Laser Absorption Spectroscopy and Light Emitting Diodes

Laser based measurement strategies have been developed extensively in combustion and propulsion related research due to its ability to non-intrusively produce quick time-resolved measurements of gas composition, temperature, velocity, and pressure [6-11]. However, the cost and complexity of laser-based systems limits their broader applicability beyond laboratory, development, and certain industrial settings; specifically, they cannot provide a practical solution for automotive on-board diagnostics (OBD) and control. Light emitting diodes present a potential solution to development of sensors that are sufficiently cost effective and rugged for practical on-board automotive applications. The design and methods discussed here may be applied to developing a range of low-cost sensors for measuring a variety of species. Figure 2 shows the spectral absorption features of several important gases within the spectral range of mid-infrared (MIR) LEDs (available through the Ioffe Institute)[12].

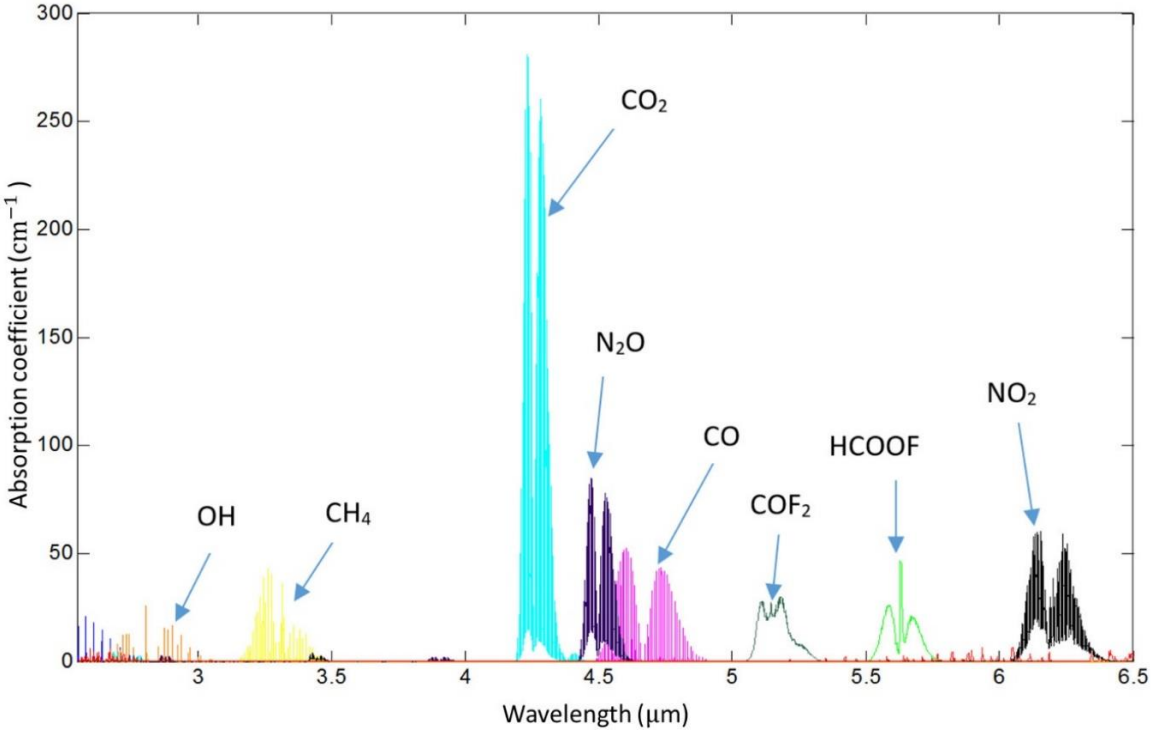

Figure 2: Absorption features of OH, H_2O, CH_4, CO_2, N_2O, CO, COF_2, HCOOF, and NO_2 in the MIR range at 298K and 1atm. Although H_2O has absorption features throughout the indicated MIR range, because they have sufficiently small magnitude in the probed region, associated interference is practically negligible.

The sensor described here has many benefits compared to existing commercially available sensors; these include response time, cost, size, applicability to integrated OBD systems, and suitability to in-situ probe measurements as vs. extractive sampling. There currently exist two main categories commercial non-dispersive infrared (NDIR) sensors for monitoring CO and CO_2. The first category includes small, compact sensors used primarily for monitoring manufacturing processes and/or in HVAC systems. While compact, these sensors have slow response times, ranging from 0.5 to 20 seconds, and most do not measure both CO and CO_2 simultaneously. The second category of commercial sensors includes large laboratory systems (e.g., Horiba MEXA-7100FX) for making time-resolved measurements via extractive sampling; while these are

routinely applied to engine research, they are bulky, not adaptable for probe-based measurements and expensive. Neither of these types of sensors are suitable for on board diagnostics, due either to their slow response time, large size and power requirements. Commercial systems exist (e.g., Horiba OBS-200) for on-road measurements of CO and CO_2 using NDIR; however, these are large (about 60 kg), primarily intended for development, do not provide a diagnostic pathway for on-vehicle OBD integration. The sensor developed in this work provides fast simultaneous measurements of CO and CO_2 in a compact and inexpensive package. Based on its similarity to a separately developed CO_2 sensor that has been configured with a remote-probe sample interface (vs. extractive sampling) and applied for on-engine measurements, the sensor described here is expected to have these same capabilities [13]. In summary, the sensor offers unique advantages compared to existing commercial CO and CO_2 sensors, is compact, inexpensive, configurable for probe-based measurements, applicable to on-engine measurements, and provides a pathway for development of OBD sensors and other applications requiring these sensor characteristics such as aviation and space exploration.

Using LEDs is not without its drawbacks, for which they will need to be accounted for and the sensor properly validated. To name a few, LEDs are spectrally broad, are not as intense as lasers, and emit incoherent light. The emitted spectrum of the LEDs spans several transitions which create uncertainty associated with interfering species such as water vapor. With lasers a transition can be picked out on the basis of strength and overlap with other species, and then targeted. The LEDs will need to be passed through a filter to narrow the bandwidth however they will remain quite broad and will lose intensity after being transmitted through. In concern for low power output, a cooled detector with high sensitivity is used for measuring the beam attenuation. It is

inherently difficult to collimate and focus to a point incoherent light, which is necessary when transmitting through the gases and focusing onto the detector, respectively. To address this, simulation software is used to optimize the lens design setup to achieve the best performance with minimal losses. Noise from interfering species and losses from non-ideal light sources are characterized and appropriate calibration is done for the greatest effectiveness of the sensor.

Organization of Thesis

This thesis is organized as follows. Note that much of the content of this thesis was also taken from my publication [14].

2) Chapter 2 discusses the Beer-Lambert law, the fundamental theory of absorption spectroscopy and diagnostics methods. Central terms and concepts are defined that will be necessary for proceeding chapters. The Beer-Lambert law is used describe absorption for spectrally narrow radiation so I continue the discussion with how this may apply to broad spectrum sources such as LEDs and how absorptions for such sources could be modelled. This chapter is concluded with band selections for CO and CO_2 for the sensors operation.
3) Chapter 3 details the design of the sensors including comparison of infrared sources, component selection and characterization, configuration, and simulations. LEDs are compared with other broad spectrum sources and justified for selection. The operating parameters are also outlined including cooling temperature and modulation frequencies. The detector is characterized for suitability for the LEDs. Optical train simulations that were conducted using the Zemax software to optimize signal are discussed. Thermal management, electoral circuit, and the sensor's DAQ are also discussed here.

4) Chapter 4 elaborates on the evaluation of the sensor's performance. This chapter describes the experimental apparatuses used, experiment procedures, and results. Experiments performed include baseline detection limit at standard temperature and pressure (STP), time resolution, and performance in near space like conditions.
5) Chapter 5 wraps up the thesis by drawing conclusions and discusses future directions for the sensor.

CHAPTER 2: THEORY

Beer-Lambert Law

Absorption spectroscopy can be used to quantify the properties of a target molecular species via its characteristic absorption spectrum; these properties include concentration, temperature and pressure. For species concentration measurements, light of a wavelength overlapping that of the targeted species' absorption spectra is directed through a gas. The light attenuation, due to absorption, is measured by comparing the incident and transmitted radiation, and is related to the target species' concentration. Monochromatic absorption spectroscopy follows the Beer-Lambert law, which relates the attenuation to the properties of light and adsorbing species; specifically, the ratio of the transmitted irradiance I (W cm^{-2}) to the incident irradiance I_0 (W cm^{-2}) when a spectrally narrow radiation at frequency ν (cm^{-1}) is directed through a gas medium. Broad spectrum absorption in the linear-regime can be represented by summation spectrally integrated version of Beer's law:

$$T = \left(\frac{I}{I_0}\right) = \int E_\lambda F_\lambda \exp(-k_\lambda L)\, d\lambda, \tag{1}$$

where T (\) is the transmissivity, E_λ (unitless) is the spectral emissive profile of the LED source, F_λ (unitless) is spectral transmissivity profile of the filter, k_λ (cm^{-1}) is the spectral absorption coefficient, and L (cm) the absorption path length through the gas. The spectral absorption coefficient is defined as the product $k_\lambda = S_\lambda \phi_\lambda P x_i$ where S_λ(cm^{-2} atm^{-1}) is the line strength, ϕ (cm) the line-shape function, P (atm) is the total pressure, and x_i (\) the mole fraction of the absorbing species. For these studies, line strength values were determined from the HITRAN 2012

database which provides a compilation of spectroscopic parameters used to predict and simulate the transmission of light in the atmosphere [12].

The line-strength S of a specific absorption transition can is a function of temperature and can be expressed as:

$$S(T) = S(T_0)\frac{Q(T_0)}{Q(T)}\left(\frac{T_0}{T}\right)\exp\left[-\frac{hcE''}{k}\left(\frac{1}{T}-\frac{1}{T_0}\right)\right]\left[1-\exp\left(\frac{-hc\nu_0}{kT}\right)\right]\left[1-\exp\left(\frac{-hc\nu_0}{kT_0}\right)\right]^{-1}, \quad (2)$$

where $Q(T)$ is the partition function, E''(cm^{-1}) the lower-state energy for the transition, ν_0 (cm^{-1}) the transition's line-center frequency, T_0(K) the reference temperature corresponding to the reference line-strength, S(T_0), h Planck's constant, c speed of light, and k Boltzmann's constant.

Values for the partition function are dependent on the temperature. Here, the partition function was fitted with a cubic polynomial:

$$Q(T) = a + bT + cT^2 + dT^3, \quad (3)$$

where a, b, c, and d are the constants listed below in table 1. This polynomial was fitted to data available in the HITRAN database.

Table 1: Partition function coefficients.

Species	***a***	***b***	***c***	***d***
Water	985.1	691.5	154.2	19.51
CO	3.889	0.3489	-3.83× 10^{-6}	3.352× 10^{-8}
CO_2	2071	2058	882.4	179.4

The line-shape function ϕ was approximated with a Voigt function for collisional and Doppler broadened transitions. The collision-broadened full-width at half maximum (FWHM) of the absorbing species i is given by

$$\Delta\nu_c = P\sum_j x_j 2\gamma_{ji}, \tag{4}$$

where x_j is the mole fraction of the collisional partner and $2\gamma_{ji}[\mathrm{cm}^{-1}\ \mathrm{atm}^{-1}]$ is the broadening coefficient of j with i. The broadening coefficient $2\gamma_{ij}$ is known at a reference temperature T_0 and scaled as follows:

$$2\gamma(T) = 2\gamma(T_0)\left(\frac{T_0}{T}\right)^n, \tag{5}$$

where n is the temperature coefficient. The air- and self-broadening coefficients were also attained from the HITRAN database. Tests performed to validate the sensor are conducted in air however shock tube experiments are planned which may require investigation of collisional broadening from argon or other gases.

Mixed-Regime Broadband Absorption

For broadband absorption, many hundreds or thousands of individual absorption transitions may exist within the probed spectral region, which can lead to mixed-regime absorbance beyond the linear regime absorbance described by Eq.1; i.e., stronger transitions may begin to saturate at certain CO and/or CO_2 concentrations while weaker transitions may remain in the linear-regime. This mixed-regime absorption is depicted in Figure 3 below, which shows the normalized filtered emission of an LED (red) and the absorbed LED emission (blue). With a pathlength of 7.97cm and

a concentration of 0.2% CO2, several of the stronger transitions have saturated (bottomed out to zero emission) so that they are completely absorbed the LEDs emission at that wavelength and no longer contribute to the sensitivity of the of sensor. As will be seen, this creates a non-linear response above a characteristic concentration where the major absorption transitions move from the linear to saturated regime. Yoo et al. [13] discuss curves-of-growth theory, typically applied in stellar atmosphere spectroscopy, as potential model for such mixed-regime absorbance. In the analysis presented here, curves of growth are used to estimate line shape parameters as the spectral resolution is not sufficient to resolve individual transitions, and mixed-regime absorption certainly occurs.

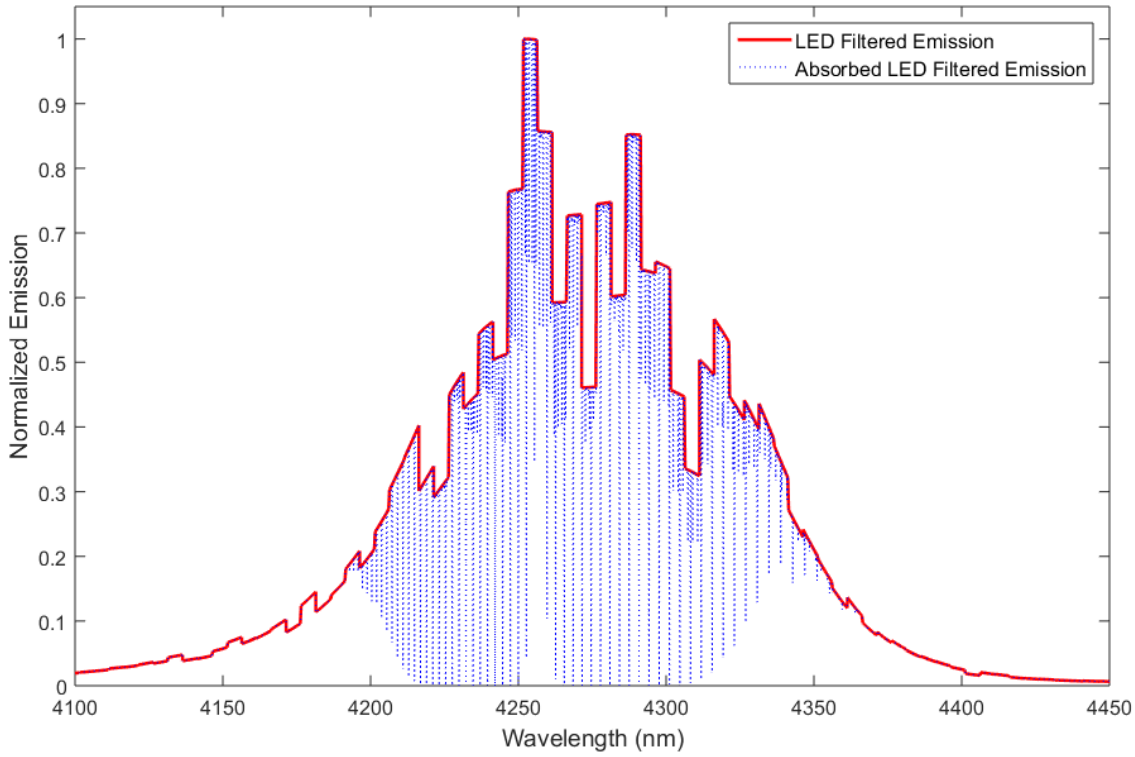

Figure 3: Mixed-regime broadband absorption of 0.2% CO_2 at 298K and 1 atm with a pathlength of 7.97cm. Saturation occurs where the absorbed LED emission bottoms out at zero (it is completely absorbed by the gas transition).

Low Pressure and Temperature Absorption

From equation 1 it can be seen that the absorption strength of the gas is directly proportional to the pressure of the gas is under, so in near space conditions we can expect reduced signal. From equation 2, we can see that the strength of absorption is also a function of temperature however this not nearly as strong and lower temperature will generally average out to increase absorption strength. Figure 4 below compare the absorption features of CO2 at standard temperature and pressure (STP) of 296K and 1atm with near space conditions of 1/100atm and 256K.

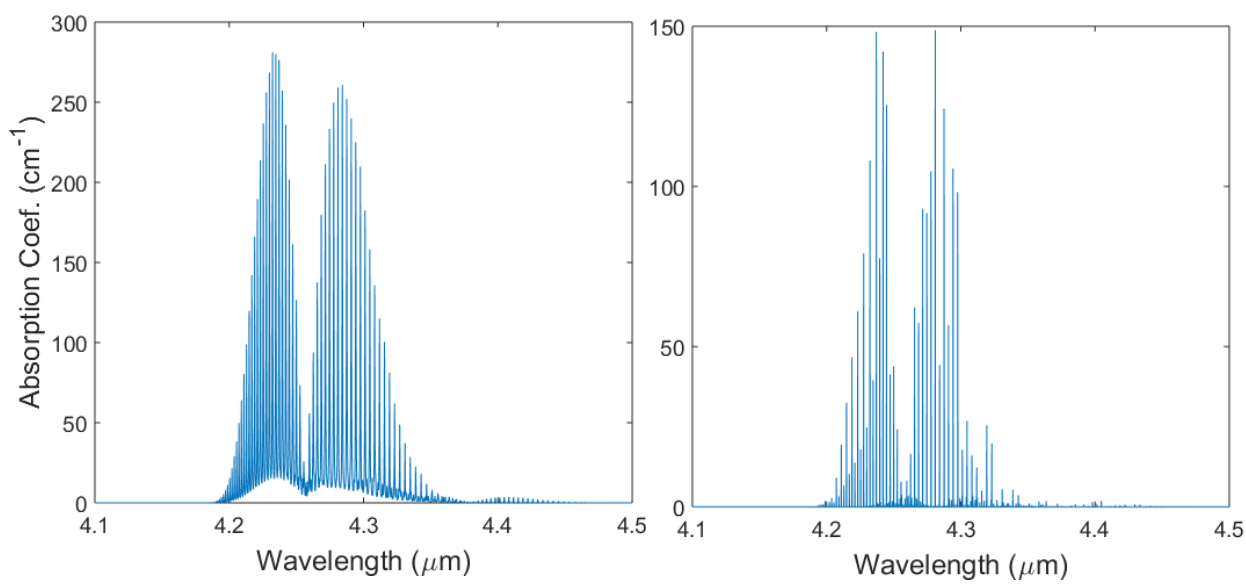

Figure 4: Comparison of absorption features of CO2 at STP (left) and near space conditions (right). Absorption strength at near space may be halved or less.

Method of Application

A fixed-wavelength direction absorption with amplitude modulation method will be used in applications of this sensor, which infers gas concentration directly from Beer's Law (eqn. 1). For this the incident, or baseline, light I_0 must be known which, due to the low cost of LEDs, a separate light source can be used that is known to have no or little interference from expected

gases. Using this method, quick measurements can be made with the bandwidth being limited only by the sampling speed of the detector or data acquisition unit (DAQ).

Band Selection

The wavelengths that are available using MIR LEDs range from 1.52 to 7μm. Figure 5 shows the absorption spectrum of CO_2, CO, and H_2O in this range. The largest band for CO_2 is around 4.2μm. CO has the greatest absorption around 4.7μm. H_2O has very little presents in this area. These bands will allow for the greatest resolution using this technique and the strong absorption will help compensate for the low power output of the LEDs.

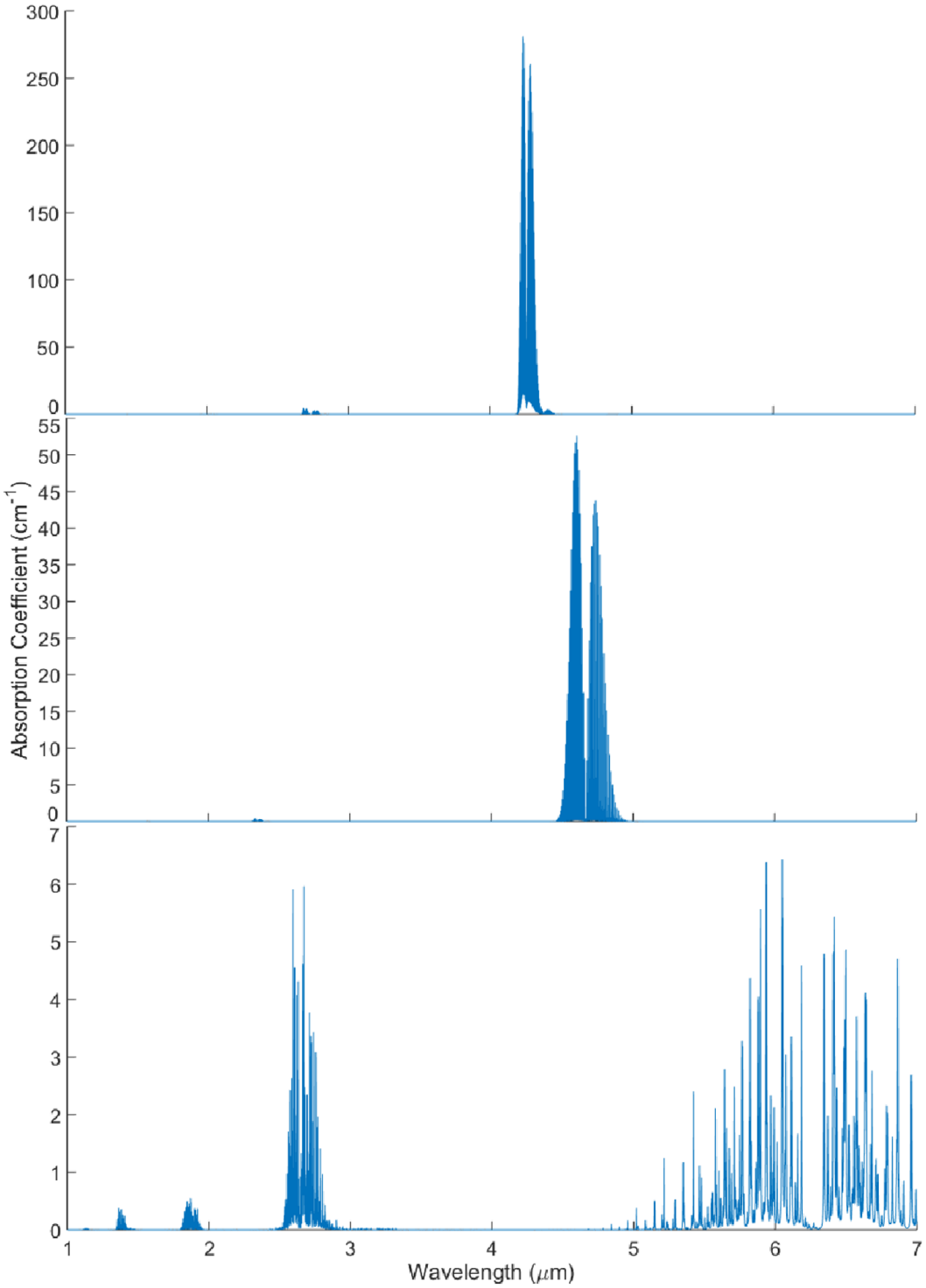

Figure 5: Absorption spectrum for CO2 (top), CO (middle), and H2O (bottom) from 1 to 7um at 296K and 1atm.

CHAPTER 3: SENSOR DESIGN

Infrared Source

In chapter 1 I presented the advantages of using LEDs over the more conventional lasers, though this was more of a discussion on NDIR versus laser absorption spectroscopy (LAS). There are a few low-cost, broad spectrum sources that have similarly appealing features to LEDs. Here I will compare those with LEDs and along with the pros and cons of each. By far the most commonly used source is the tungsten filament bulb (micro-bulb) as it cheap and has a high output. Another currently emerging technology is thin foil element infrared sources which work by heating a very thin film of metal (titanium or platinum alloy) to ~1000°C then letting it radiatively cool.

Currently, micro-bulbs dominate the market for NDIR sensors. While their relatively high output and low cost has afforded them success is basic consumer market, their limitations of having high drift, low efficiency, low modulation rates, and limited spectral range prevent their adaption to the more specialized markets discussed here. The micro-bulb operates by heating a tungsten filament inside of a glass envelope to temperatures ~3000K which causes the filament to evaporate over time. This causes the output of the bulb to drift significantly which then requires regular calibration of the sensor to offset. The high operating temperature also makes the bulb inefficient compared to the LEDs making it less appealing for low-power jobs. Finally, micro-bulbs are limited to modulations rates of only a few hertz where the LEDs can be modulated at rates as high 50MHz. This makes micro-bulbs unappealing for situations demanding high time resolution.

Infrared foil elements provide similar magnitude intensity output as micro-bulbs however provide greater spectral range and slightly faster modulations rates due to smaller thermal mass

[15]. They are, however, still limited to no more than ~1kHz modulation rate which makes them ill-suited for EGR measurements which require speeds >10kHz [16]. I have not been able to identify any studies on life-time output of these sources.

The selection of MIR LEDs for the source came down to their very low-power consumption (<1W) and very stable output (>20000hrs) [17]. LEDs cost is slightly greater than the other sources however for the applications being considered the cost is still considerably low. While the I did not take advantage of the speed of the LEDs in my work, it worth mentioning that this is a very strong advantage for LEDs which could allow them ultra-fast measurements in the MHz range. The main drawback of LEDs is their lower output however this can be met with certain design decisions such as longer/folded pathlengths.

Component Selection and Design Details

This sensor utilizes three LEDs to cover three different wavelength regions: a reference LED (I_0 in Beer's law) centered near 3.6μm, one near 4.2μm for detecting CO_2, and one near 4.7μm for detecting CO. Figure 6 shows the normalized spectral profiles of these LEDs overlaid with the absorption features of CO and CO_2; it is clear from Figure 6 that the LEDs are spectrally broader than the individual absorption transitions, and that the associated measurements will be the integral of absorption from many individual lines in the indicated bands. Figure 6 also shows the spectral profiles of source-specific band-pass filters selected to narrow the bandwidth of the LEDs; these reduce spectral overlap between the three LEDs, and associated cross interference. The CO2 filter has good overlap with the CO2 absorption features however the CO filter happens overlap a valley in the its absorption features which hurts its already weak signal. I have since

acquired a new filter that give greater overlap however there was not sufficient time to characterize it.

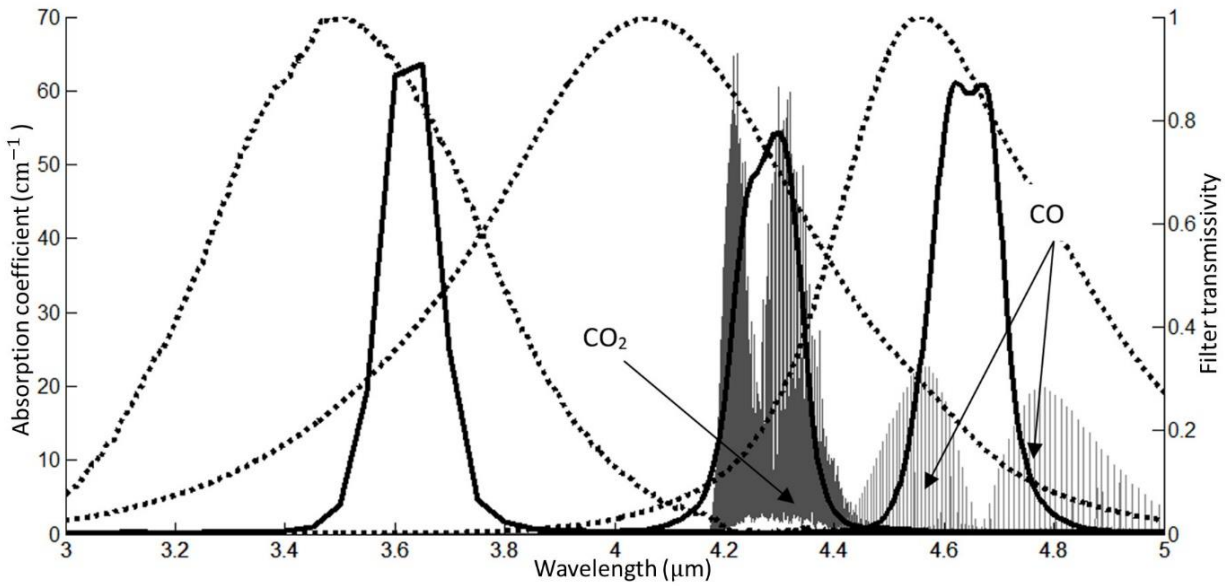

Figure 6: Normalized spectral profiles of the LEDs (dashed lines) and filters (solid lines). The absorption features of CO_2 and CO are shown (296K) to illustrate spectral overlap between the LED emission, filter transmission, and absorption features.

The output of the LEDs (spectrally and in intensity) is dependent on their temperate so to achieve a steadier and more consistent output performance, each LED was individually temperature controlled (to -10 $\pm$0.2°C) using a two stage thermal electric cooler (TEC). The temperature dependent spectral characteristics of one of the LEDs (3.6μm) is shown in Figure 7 below [18]. For typical room temperature operation, the TECs can be operated to created temperature difference that cools the LED (~$-$10°C) and rejects heat to a heat sink (~26°C). When operating at lower temperatures expected in various space vehicle environments (-15 to -50°C) the poles on the TECs are switched so that they actively heat the LEDs instead. For this case it may

be necessary to supply a thermal pool for the TECs to draw from in order to sufficiently maintain LED temperature.

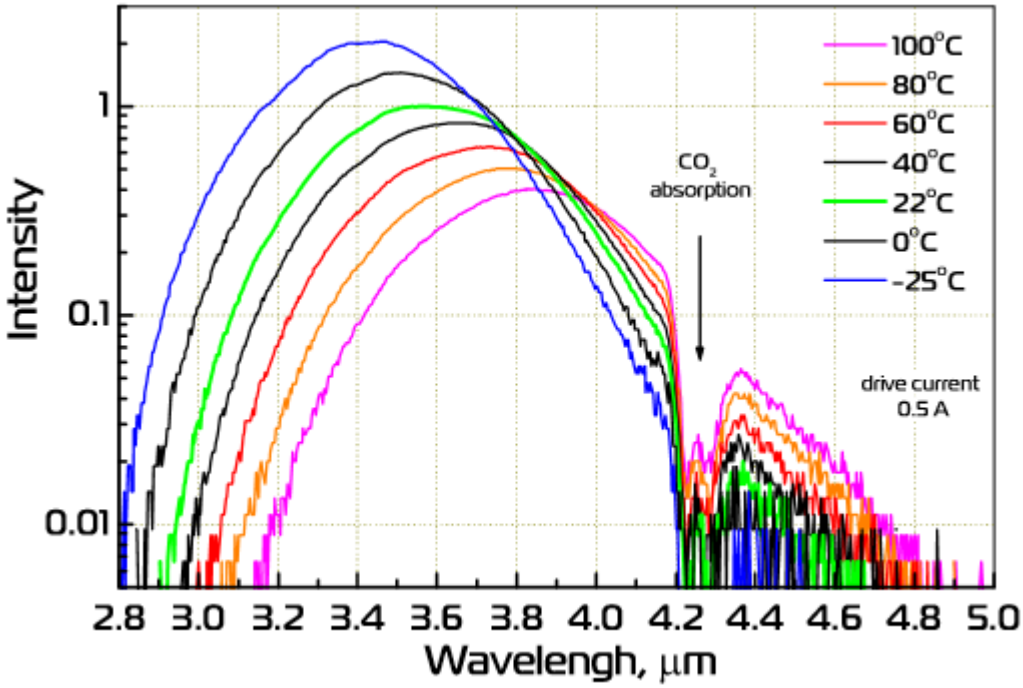

Figure 7: Emission spectral of the 3.6μm LED at different temperatures [18]. Lowering the temperature of the LED does increase output but this must be balanced with power constraints and temperature stability. It is much more critical to have a stable temperature than increased output.

Using a single detector for the three LED signals reduces instrument cost and complexities associate with multiple detectors; e.g., accounting for detector-specific response, dark current, noise and other characteristics. This single-detector approach requires the three LEDs to be combined into a single measurement beam. The LEDs were individually collimated, filtered with the appropriate band-pass filters, and combined using two Pellicle beam splitters as shown in Figure 8. The beam splitters have their own spectral characteristics (table 2) so the arrangement of the LEDs were optimized so that the 4.7μm LED, which has lowest intensity output, lost the least

amount of signal and the 4.2μm was optimized secondly. The output of each LED was modulated at a unique frequency by a dedicated function generator or DAQ unit, using a square-wave unity-duty-cycle function; i.e., the 3.6µm, 4.2µm and, 4.7µm LEDs were modulated at 55, 77 and 115 kHz, respectively. The signal corresponding to each LED was determined from the Fourier transform of the combined single-detector signal as that at the corresponding modulation frequency. A Vigo Systems three-stage TEC photovoltaic detector (model PVI-3TE-5, Boston Electronics) with an STCC-04 TEC controller (from the same manufacturer and source) was used. This detector has fast response and high sensitivity to radiation between 3 and 5µm.

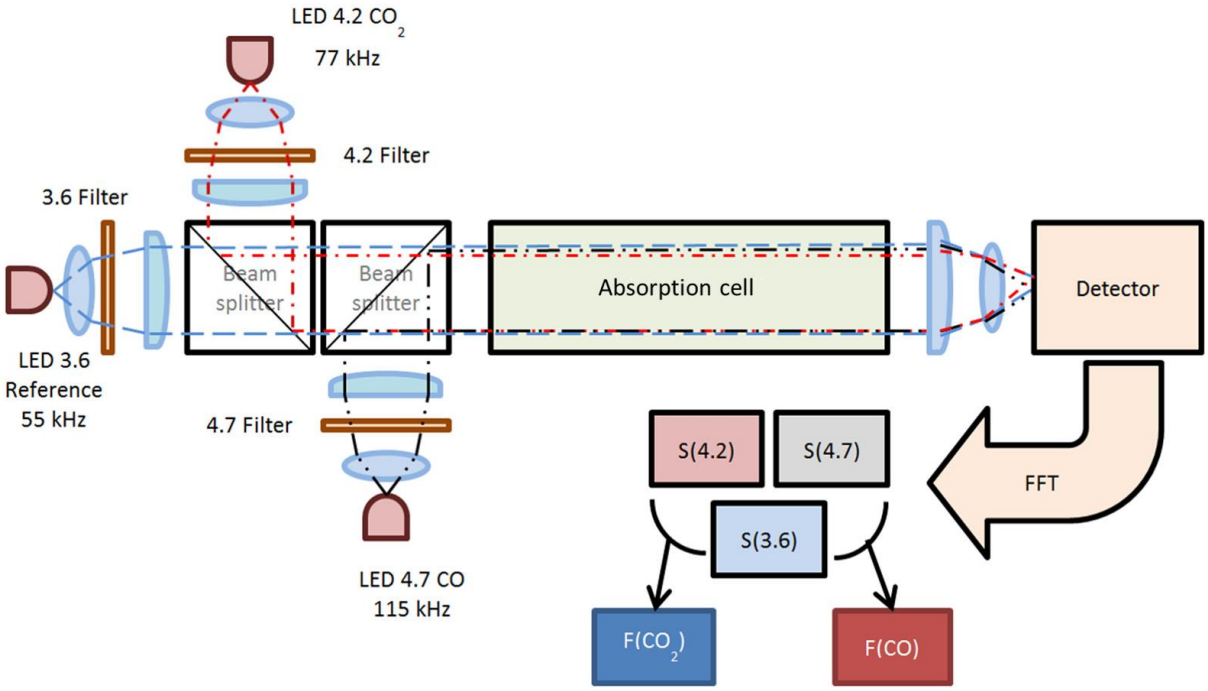

Figure 8: Sensor hardware and processing schematic including measurement flow cell.

Table 2: Pellicle beam splitter transmittance/reflectance.

LED Center Wavelength (μm)	**Reflectance (%)**	**Transmittance (%)**
3.6	33	67
4.2	45	55
4.7	48	53

The catch is simply the detector and lenses to focus the beam from the light guide into detector. The detector selected is a Vigo Systems three-stage-thermoelectrically-cooled (TEC) photovoltaic detector (model PVI-3TE-5). An STCC-04 TEC controller from the same manufacturer is used detector temperature control. Further specifications for these instruments can be found in appendix. The detectability D^* of the detector is defined as:

$$D^* \equiv \frac{\sqrt{A \times \Delta f}}{NEP} = R_v \frac{\sqrt{A \times \Delta f}}{V_n}, \tag{6}$$

where A is the detector area in cm^2, Δf is the signal bandwidth, V_n is noise voltage, R_v is the voltage responsively of the detector, and NEP is the Noise Equivalent Power [19]. NEP is the optical input power to the detector that produces a signal-to-noise ratio of unity (S/N = 1). For this detector $A = 0.01\text{cm}^2$ and $D^* = 10^{11}$. The optical signal at intermediate frequency due to optical power P and power of radiation of local oscillator P_L is $V_I = R_v(2PP_L)^{1/2}$. NEP is the optical power that generatred the signal equal to noise voltage V_n, so

$$NEP = \frac{V_n^2}{2P_L R_v^2}, \tag{7}$$

Solving for R_v in equation 6 and substituting into equation 7:

$$NEP = \frac{A\Delta f}{2P_L D^{*2}}, \tag{8}$$

The lowest expected LED power output (from the 4.7μm LED) is around 2.5×10^{-7}W. For a bandwidth of 79kHz, $NEP = 1.5 \times 10^{-13}$W. That is an optical power output greater 1.5×10^{-13}W is necessary to be distinguishable from noise, which is sufficient for the selected LEDs.

Optical Train Optimization and Simulations

In order to optimize sensor performance, the spatially extended incoherent LED emission must be carefully coupled into and within the system. Optical-design software (Radiant ZEMAX) allowed simulation of the entire sensor optical system, and was used to optimize the optical configuration[20]. My findings using this software was that multiple collimating lenses and multiple focusing lenses would be needed in order to get an acceptably collimated beam and to focus it to a sufficiently small point for minimal losses. First I will compare single lens design with multi-lens design then I will present the optimal lens configuration and estimated signal losses.

The sensor utilizes three LEDs which must combine into a single beam. Each LED must be collimated, combined with the other lights, and then focused to a point; while each LED has different collimated beam pathlengths depending on how many beam splitters it must pass through. This has been a vital part of the designing processes given the inherent difficulties in focusing to a point an incoherent source such as LEDs; a significant amount of power can be loss when attempting to focus the light to small point, a 1x1mm square for the case of my detector.

The Figure 9 and Figure 10 below show a one collimating lens, one launch lens setup vs. a two collimating lens/two launch lens approach for the pitch setup. In these simulations the LEDs are focused into a hollow waveguide (HWG) with an inner bore of 1mm. The detector face is placed at the immediate end of the HWG so the results shown are effectively what would be

captured by the HWG. It is clearly seen that with the second design a much more collimated beam was achieved, which resulted in less power loss as the light is transmitted through the beam splitters and combined with the other LEDs. The squares here show the irradiance on the detector face as I have described. Each square is 6mm by 6mm however only the light within the 1mm inner bore of the HWG will reach the detector face. Notice that with design two the beam was focused to a smaller, more power dense point. With a 1mm inner bore diameter of the HWG most of our signal is being lost at the entrance of the light guides, so the smaller point is desired. Going from design one to design two the efficiency increased at the HWG entrance from 84% to 98%.

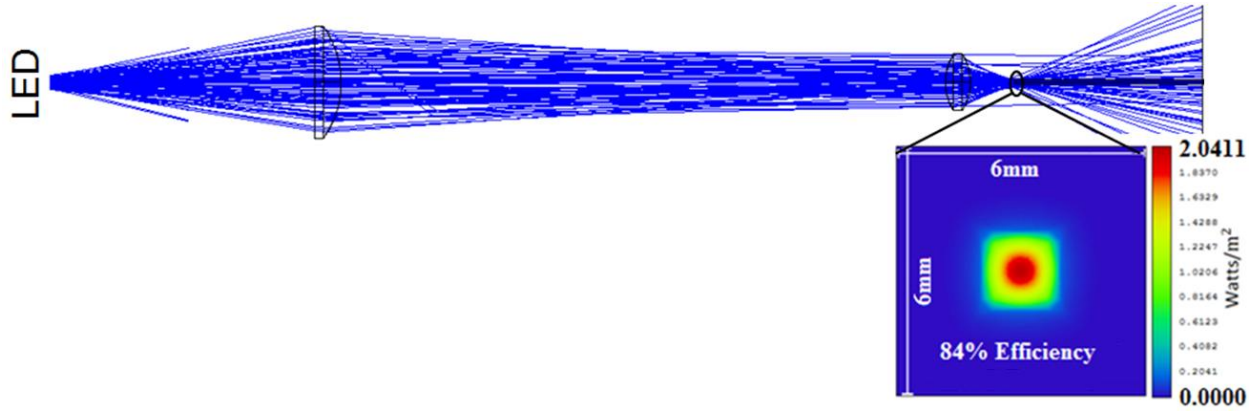

Figure 9: Pitch lens design one. A one collimating/one launch lens design for the pitch setup.

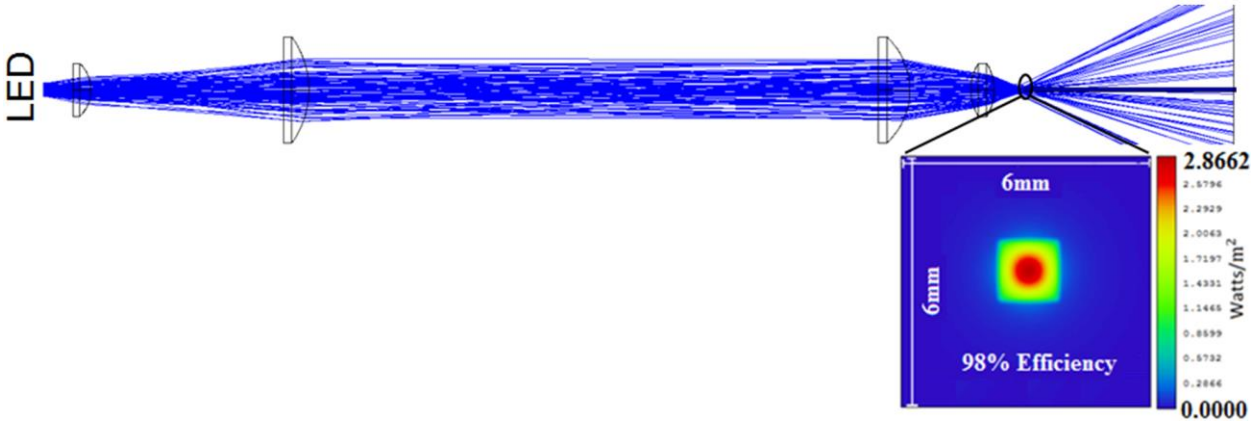

Figure 10: Pitch lens design two. A two collimating/two launch lens design for the pitch setup.

Figure 11 shows a simulation of the 3.6µm LED as it is nominally collimated, transmitted through the beam-combining optics and measurement cell, and focused onto the detector; this reflects the design configuration implemented in these studies. The LED beams were nominally collimated to minimize signal loss from vignetting or clipping by hardware surfaces during its travel through the sensor system; two plano-convex lenses (20mm and 50mm focal length CaF_2 lenses from Thorlabs) produced a semi-collimated beam with a working diameter (i.e., between the collimating and focusing lens sets) of ca. 12.7mm. Following transmission through the measurement cell, a plano-convex lens coupled with a bi-convex lens (40mm and 15mm focal length CaF_2 lenses, respectively) was used to focus the combined three LED beams onto the 1-mm^2 square detector; i.e., although each LED has a dedicated collimating lens set, they have a common focusing lens set as indicated in Figure 8.

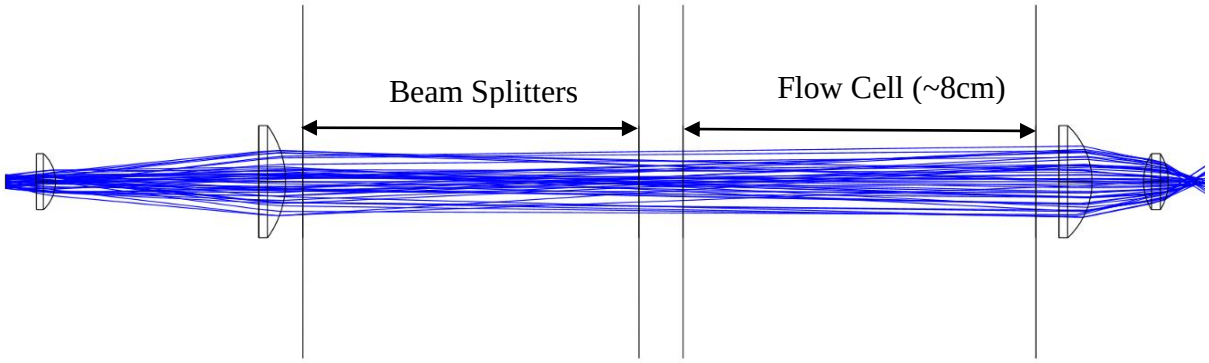

Figure 11: Simulation of the entire beam path for the 3.6µm LED emission, which has the longest optical path. The beam splitters and absorption cell has been drawn in with approximate proportions for reference only.

Figure 12 shows the simulation detector face for this configuration with a 1x1mm surface, the same dimensions as the Vigo Systems detector used in my setup. The simulations suggest that an optical efficiency of 45% may be possible with this configuration, though this does not include losses from beam splitters, bandpass filters, windows, or atmospheric gas absorption. In total, I estimate that only south of 1/3 of the LED emission is captured by the detector, reflecting the challenge of collimating and focusing the emission of spatially extended incoherent sources to a small area. Even with these significant losses, we demonstrate significant instrument performance as will be described below. Future work will focus on optimizing the optics, with the potential of doubling the signal and realizing corresponding diagnostic benefits regarding signal-to-noise ratio, temporal resolution, and detection limit.

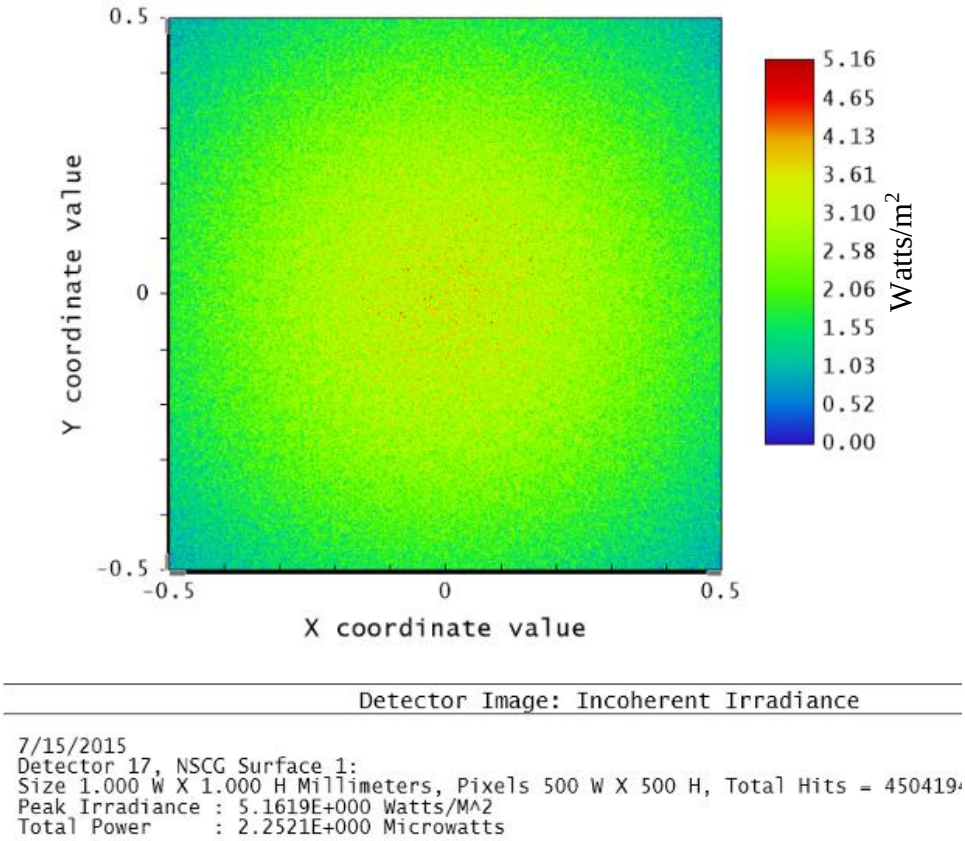

Figure 12: Simulation detector face. The source had a total output of 5 microwatts so optical efficiency is 45%. This not include losses due to beam splitters and bandpass filters which can bring losses south of 1/3.

Driving Electronics

Original testing of this sensor started by using function generators to drive the LEDs however I suspected that these did not supply sufficient current. Driving the LEDs at max specifications (pulsed power) requires ~0.45V at ~1A. To meet the current demands of the LEDs, Wavelength Electronics WLD3343 general purpose drivers were acquired (specs in appendix). These were eventually adopted to drive the TECs for the LEDs as well. In Figure 13 below the output from the LEDs while driven from the function driven vs those driven by the WLD3342 modules is compared. Note that each LED was modulated at a different frequency in these test sets

however all else was equal. The output the 3.6μm LED was increased by 78.9 times, the 4.2μm LED was increased by 13.5 times, and the 4.7μm was increased by 6.1 times.

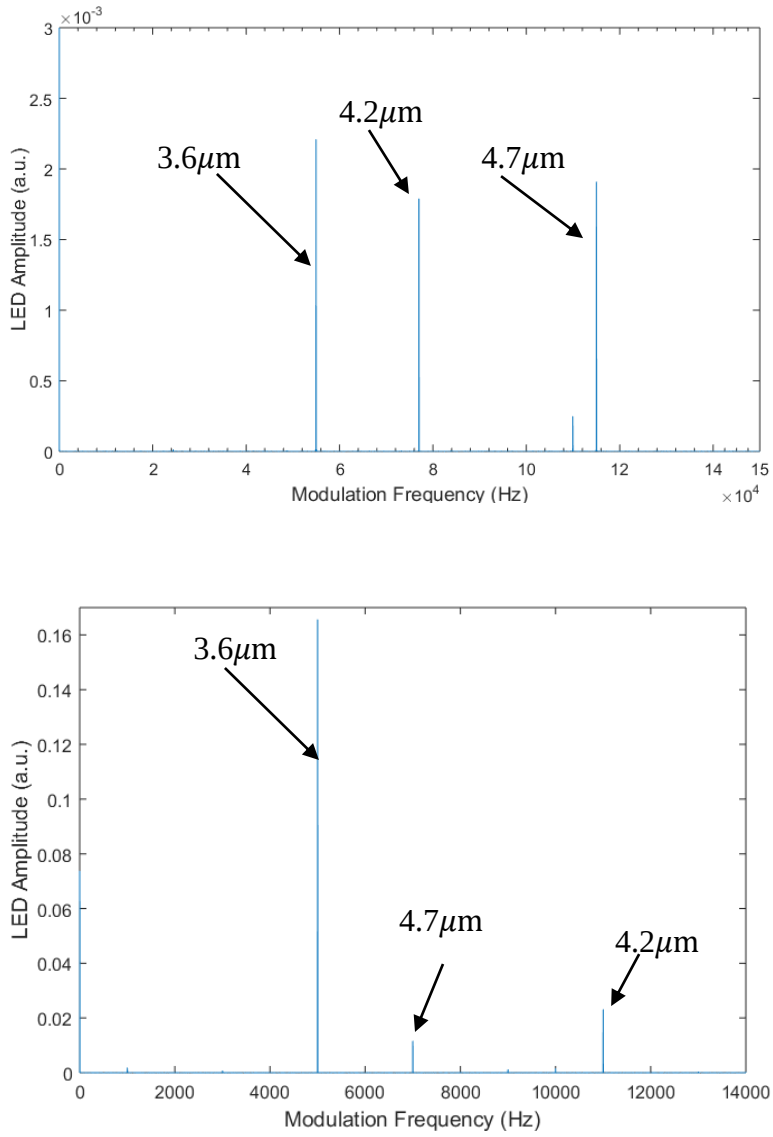

Figure 13: LED output comparison for upgraded circuit. (Top) LEDs driven with SRS DS345 function generator. (Bottom) LEDs driven with Wavelength Electronics WLD3343 general purpose driver modules.

The WLD3342 modules allow use to properly drive the LEDs properly as well as power them using batteries, which is will be critical on high altitude balloon flight. However, there have

been a few drawbacks that have been observed. First, their output appears to be proportional to their power source voltage supply so if they are being power by batteries, their current output with decline steadily as the batteries supply is drained. This is particularly an issue due to the second issue which is: they are very inefficient. They produce significant amounts of heat and thus are large load on the battery cells. Furthermore, this heat can build up if it is not sufficiently dissipated causing he modules to overheat. Future iterations should consider more efficient current regulators.

Thermal Management

While this sensor is designed to operate in multiple environments, the greatest challenges in thermal management is operation in low pressures as heat rejections is great reduced due to low heat convection efficacy. As previously mentioned, the LEDs and detector are equipped with TECs which can be used to cool or heat the component. For the detector, we are only interested in cooling since its operating temperature is below all environmental temperatures being considered (detector operating temperature is -60°C). The LEDs and detector are very small masses and require very little to maintain their temperature. A small aluminum mass is used as a thermal pool for the LEDs in both standard and low pressure conditions, which is shown below in Figure 14. Since the TEC are only turned on for very brief periods of time, the thermal masses are able to dissipate or absorb heat as needed at a sufficient rate. This setup is validated and discussed in chapter 4.

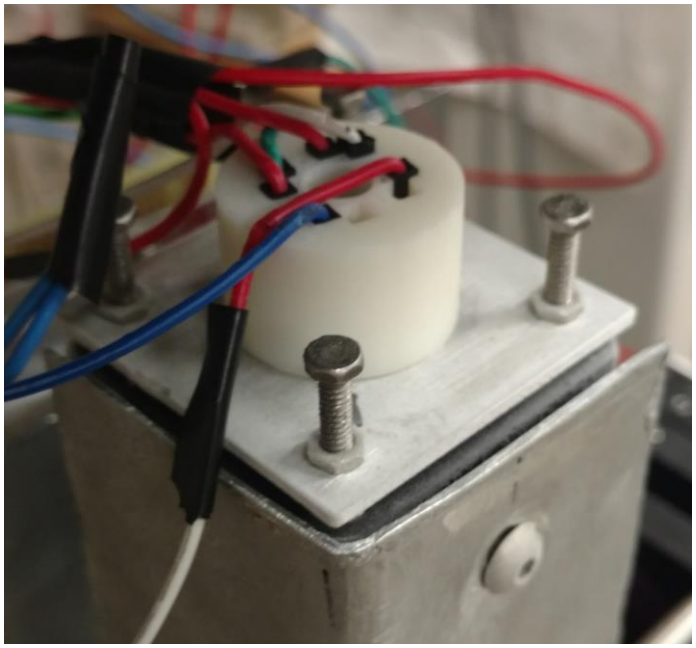

Figure 14: The aluminum mass for the 3.6μm LED. You can also see the 3D printed wire connecter here.

DAQ Control

A National Instruments cRIO-9031 DAQ is used for data acquisition and control the sensor and its components. This was selected as it is a self-contained and robust DAQ system which will allow for battery operation in through the varied environments testing is planned. Specific tasks of the DAQ include: detector data logging, LED signal function generation, and LED temperature control. All of these tasks can be performed headless, that is autonomously without the intervention from a user. Figure 15 below shows the architecture of the DAQ's code or virtual instruments (VIs).

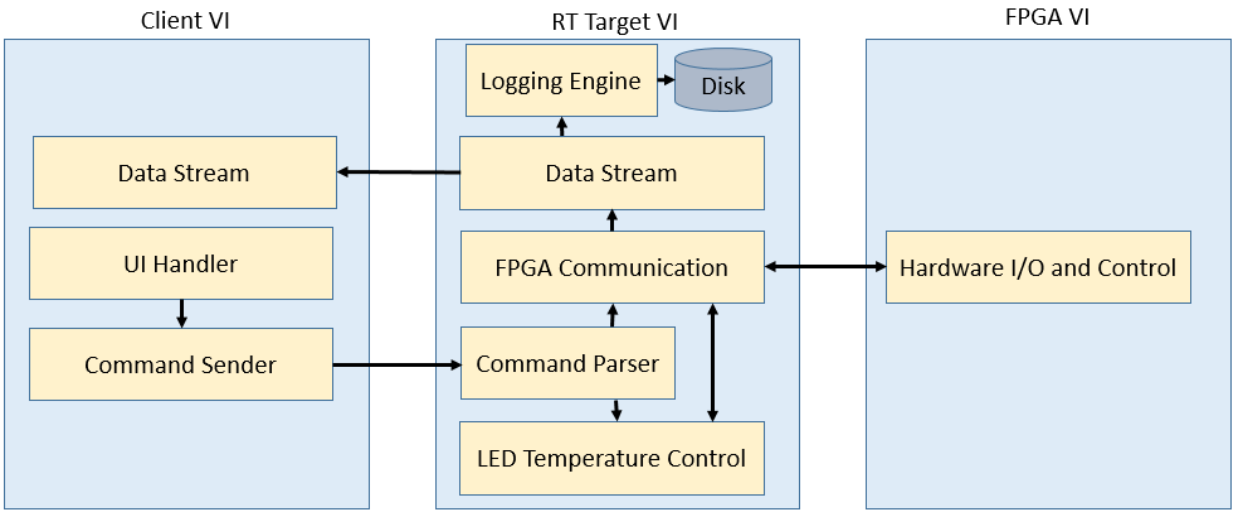

Figure 15: The sensor DAQ architecture consists of two base virtual instruments (VIs) and a third client VI for diagnostics. The real-time target (RT Target) VI handles all the computation.

There are three VIs, one that runs on the DAQ's field programmable gate array (FPGA), one that runs on the DAQ's real-time host CPU, and one that runs on the user's computer. The last VI is optional, it is not necessary for the operation of the sensor and is only used for real time diagnostics and control. It allows a user to view various graphs related to the sensors performance so that they may make adjustments for its optimal operation. If no computer is attached to the DAQ, this VI does not run. The FPGA VI is a highly efficient code that's sole purpose is to control input and output from the DAQ. All data handling and manipulation is handled on the DAQ's host CPU and the RT Target VI. The main tasks here include FPGA communication, data logging, and temperature controls for the LEDs. While client operated, the user can save date at a specified length of time and append a comment to the data file. When operating headless, the DAQ will save data at a specified time interval with the last set settings. For the temperature controls of the LEDs, a simple on/off control loop is used since the LEDs have such low mass. This was able to maintain

the LEDs temperatures within $\pm 0.2°C$. The poles for each LED TEC were switch using relays which were controlled using digital IO from the DAQ.

The greatest challenge with programming the DAQ was streaming the detector signal from FPGA to the host CPU, then creating a lossless buffer of the data that was ready for when the client was ready to save the data. The DAQ samples the detector at 100kS/sec which is streamed from the FPGA to the host CPU with a direct memory access (DMA) first in first out (FIFO) data stream. On the host CPU end a circular buffer is created that is two times greater than the save duration (usually one second). When a save is made, data is allowed to be lost during the save process. The DAQ code (VIs) are in Appendix II.

Overall Design

The lab grade hardware that has been used for much of the testing described in this work is shown below in Figure 16 below. In this figure you can clearly see the detector (blue box at the bottom) and the focusing lens plates leading up to it, as well as the PVC gas cell which will be described in the next chapter. The pitch hardware is covered up by a plate that prevents misalignment and some protection from foreign objects from damaging the sensitive beam splitters. However, you can still see where each LED is by the 3D printed connector terminals and their aluminum thermal masses.

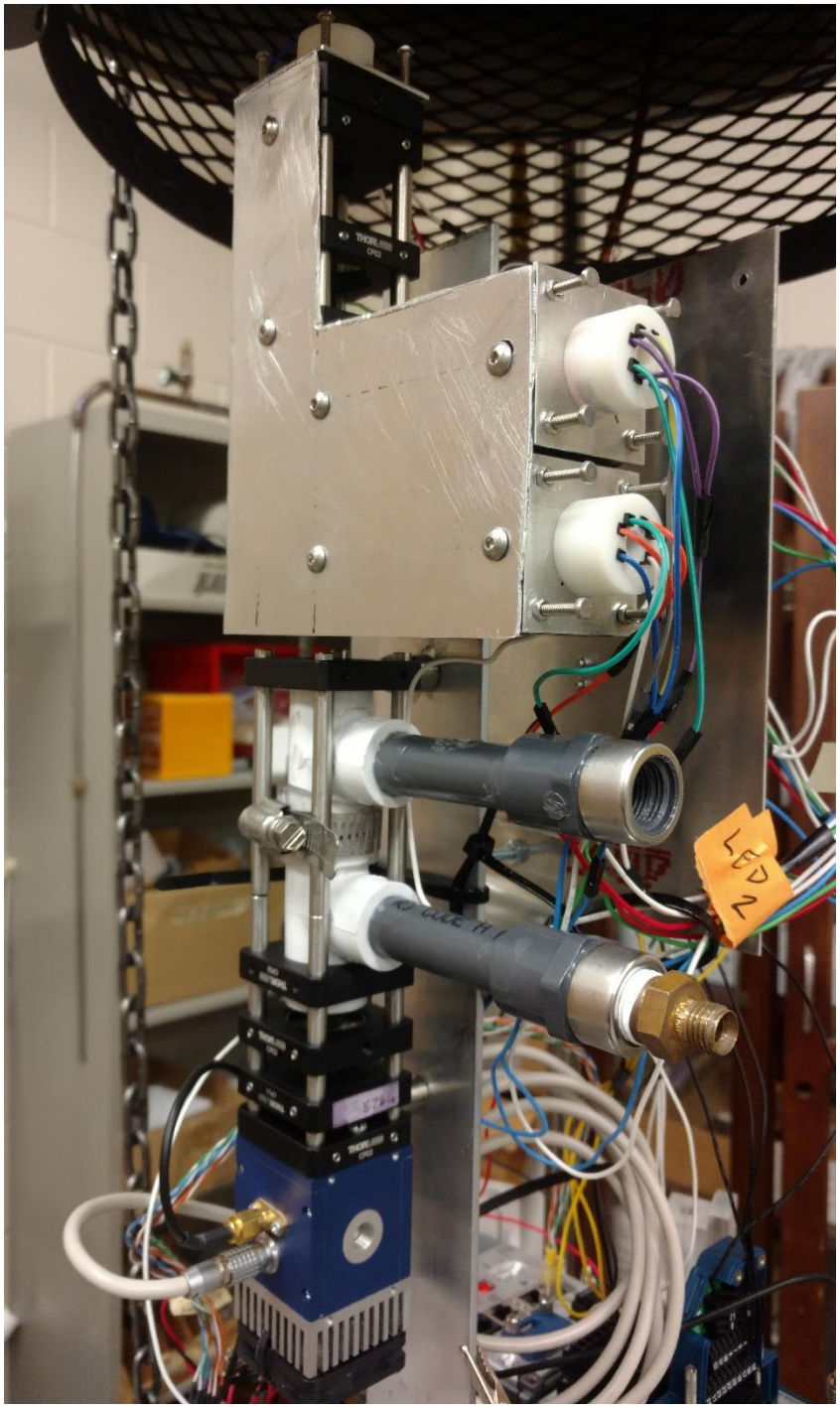

Figure 16: Overall lab sensor. From top to bottom: LEDs and pitch optics, PVC flow cell, focusing lenses, detector.

In Figure 17 below you can see a render of the balloon package that will be used for evaluation of the sensor at near space conditions. To protect the sensors sensitive electronics from the balloons telemetry, the DAQ and driving circuits will be housed in an aluminum box. The exposed wired you see in Figure 16 above will be replaced with coaxial cables if it is outside of the aluminum package. The DAQ will be secured to an aluminum frame inside the package. Construction of this system has begun and must be ready by mid-June for its flight in September.

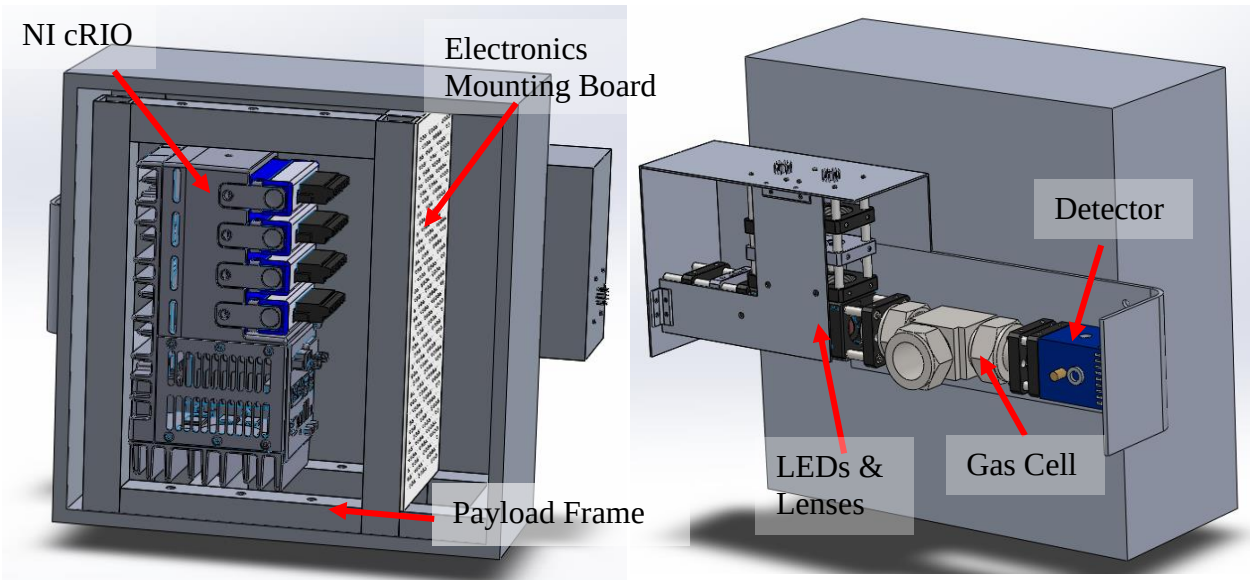

Figure 17: Sensor flight hardware. (Left) Interior of the package will contain components sensitive to electromagnetic interference (EMI) which will primarily include the DAQ and driving electronics. (Right) The sensor will be mounted to the exterior of the package.

CHAPTER 4: VALIDATION TESTS

Experiment Apparatuses

For validation and calibration of the absorption sensor, a simple flow cell was constructed out of PVC pipe that is shown in Figure 18 below. The cell simply functions to allow the flow of gases while also giving optical access. Gas flow access given by the two dark gray perpendicular PVC tubes while optical access runs parallel to the flow. The white section is essentially two PVC tees with sapphire windows glued in one end, gas access in the perpendicular port, and the other end is connected by a nylon tube that is secured with a hose clamp. This allows the length of the cell to be increased. The minimum length is 7.97cm which is the length throughout this study. This cell also has a solenoid valve equipped to it which was intended for time-resolution study how this was never used and instead a different approach was taken.

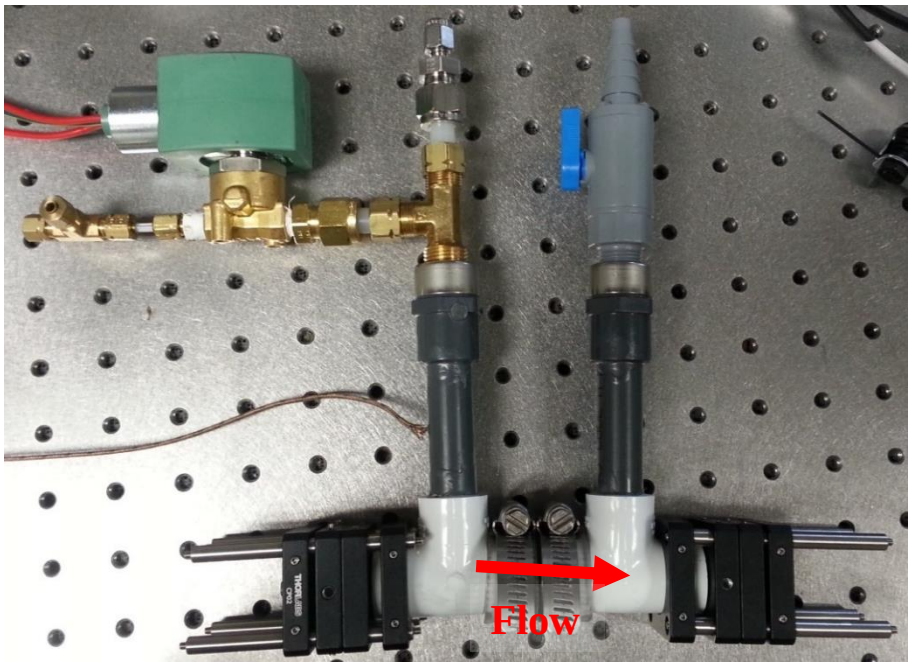

Figure 18: Simple flow cell constructed of PVC, nylon tubing, and sapphire windows.

An environmental chamber, which is shown in Figure 19 below, was used for evaluation of the sensor at near space conditions. The chamber was constructed by Dr. Peale et al and consists of a large steel bell jar that is 0.5m in diameter and 0.8m in height [21]. Inside the bell jar is a copper shroud wrapped in copper tubing which allows the flow of liquid nitrogen (LN_2) which cools the interior the chamber. Feedthrough lines at the base of the chamber allow electrical connections for controlling and monitoring the sensor and for feeding gas flow such as controlled CO and CO_2. A high volume roughing pump is used to pump the chamber down to approximately 2Torr and the chamber can be cooled to approximately -20°C.

Figure 19: UCF environmental chamber. The outer chamber comes down to hold a vacuum (down to ~2Torr) while the copper shroud is wrapped in copper tubing for the flow of liquid nitrogen (LN_2) to cool the system to low temperatures.

Detectability Limit, Cross Interference, and Simultaneous Measurements

The sensor performance was evaluated using neat gas mixtures to quantify species response factors, noise and detection limits, and cross interferences. The flowing measurement cell (cf. Absorption Cell in Figure 18) was constructed from PVC tubing, had sapphire windows, an 8-cm long absorption path length, and tubing connectors on each end to allow flow of the measurement gases. During evaluation and applications, the sensor was placed in an N_2-purged enclosure to eliminate ambient CO and CO_2 from the free-space optical train, and errors due to additional light absorption outside the measurement cell. Neat bottled gas standards and a ten-point gas divider (STEC SGD-710C) were used to control the measurement gas composition; the standards included 1% CO_2, 10% CO_2 and 4% CO, all in N_2 balance. A secondary rotameter pair was used for some of the cross-sensitivity studies. Single-gas calibration curves were measured by diluting the standards with ultra-high purity nitrogen; CO_2 was stepped from 0% to 1% in 0.1% intervals, and from 0% to 10% in 1% intervals, and CO was stepped from 0% to 4% in 0.4% intervals. Two methods were used to evaluate cross-interference between CO_2 and CO. In the first method, the primary standard was varied as described for the single-gas calibrations, using the gas divider and N_2 diluent, and combined with an N_2-diluted mixture of the secondary standard using the rotameter pair; i.e., when CO_2 was the primary standard, CO was the secondary and vice-a-versa, and the concentration of the secondary standard remained constant throughout all of the measurements. In the second method, the CO_2 and CO mirrored each other between zero and span levels by using the gas divider with CO used as the 'standard,' and CO_2 as the diluent; e.g., as CO_2 was stepped from 0-10% while CO was stepped from 4-0%. Two measurements were taken at each gas composition setting: one while stepping up the concentration of the standard and one while

stepping down; lack of hysteresis between the two data sets confirmed that the cell reach steady state at each composition element of the calibration scan

The CO_2 and CO calibration curves from the single-gas measurements are shown in Figure 20, along with the 2-sigma (95.4% confidence interval) standard deviation curves. The measurements exhibited low variation between experiments. The non-linear calibration curves are typical of broadband multi-feature absorption[9], and deviate from the linear response that would be typical of narrow-band (e.g., laser-based) absorption. Although in future work we plan to develop calibrations based on broadband absorption theory, the Figure 20 curves can be used parametrically to convert sensor output to absolute CO_2 and CO concentration levels. The single-gas detection limits, defined as the concentration where the signal-to-noise ratio (SNR) is unity (signal = 2-sigma), were determined to be 30ppm CO_2 and 400ppm CO using the 8-cm long measurement cell; changes in the absorption pathlength would inversely scale these detection limit values. Although the intrinsic and secondary (e.g., induced by function generators, etc.) noise was similar for the 4.2µm (CO_2) and 4.7µm (CO) LEDs, the 4.2µm LED had ca. twice the emission power. Thus, the CO_2 measurements have correspondingly lower SNR, and lower detection limit; since signal is also influenced by spectral and LED parameters in relation to the sensitivity discussion below, the detection limit gain (i.e., 30 vs. 400 ppm) is much greater than the power difference between the two LEDs.

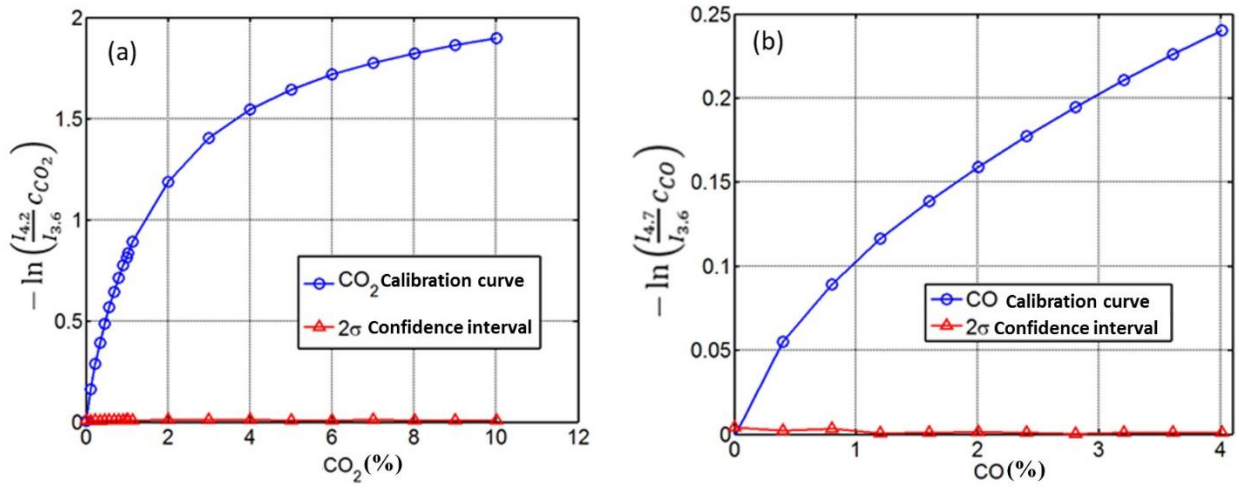

Figure 20: Calibration results for (a) CO_2 and (b) CO in the 8cm calibration cell. Values of $-\ln\left(\frac{I}{I_0}c_i\right)$ are plotted against the controlled feed CO_2 and CO concentrations.

The measurement sensitivity is indicated by the local slope of the calibration curves as shown in Figure 21, which indicates the sensor is more sensitive to CO_2 than CO throughout the CO calibration range. The difference in sensitivity and detection limit between the two gases is attributed to the probed spectral absorption features and LED-filter nature. As shown in Figure 6, the CO_2 absorption features are much stronger than those of CO, and the spectra and LED-filter bandwidth are such that a greater number of CO_2 absorption features are measured compared to CO. This causes the sensor's CO_2 sensitivity to be greater than that for CO. Figure 6 shows that many long-wavelength CO transitions within the 4.7μm-LED emission were rejected by the bandpass filter; the CO sensitivity could be correspondingly improved by using a different filter which incorporated these additional transitions into the CO measurement. For typical narrow-band absorption the sensitivity would be approximately constant and would be proportional to the spectral absorption coefficient of the targeted transition. The decreasing sensitivity with increasing concentration is due to the stronger transitions becoming saturated; as saturation progresses, the

specific absorption changes per unit concentration change goes to zero, resulting in the continuously degraded sensitivity. In contrast to the CO_2 behavior in Figure 21, the sensor's CO sensitivity is nearly constant above ca. 1.5%, which is consistent with the measurement being based on weaker absorption features and specifically fewer lines in the saturation regime.

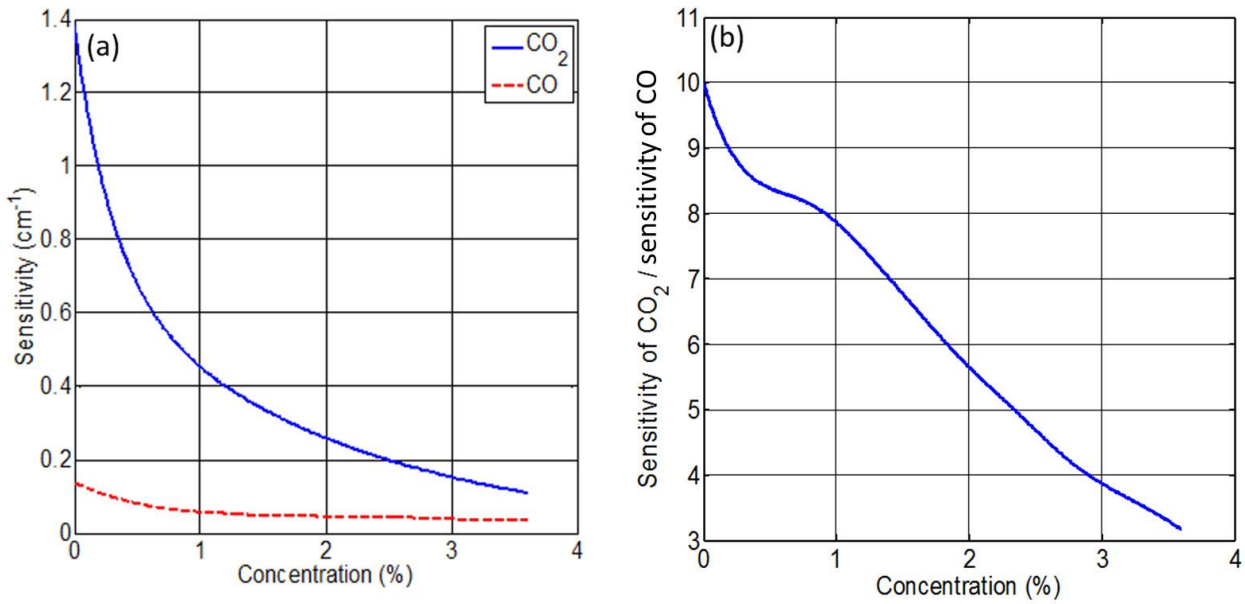

Figure 21: Sensitivity analysis of CO and CO2, based on the local slope of the calibration curves in Figure 20. The left shows the sensitivity of each species, defined as the derivative of the negative natural log of the transmissivity with respect to concentration.

Figure 22 highlights the lack of cross interferences between the CO_2 and CO measurements, by overlaying the single-gas calibration curves with those from the stepped and constant cross-interference measurements. Any cross-interference between CO_2 and CO would cause the observed signals for each to diverge from the single-gas calibration results. However, the Figure 22 indicates excellent agreement between the various calibration results, and no practical cross-interference for either CO_2 or CO.

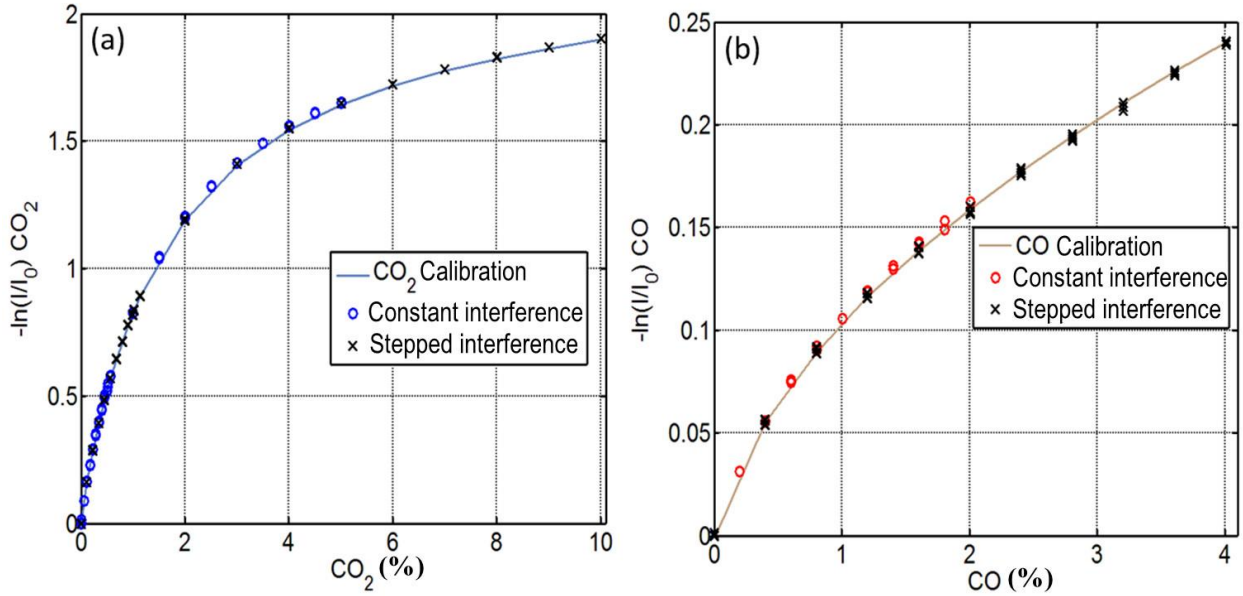

Figure 22: Results from the cross-interference measurements. The single-gas calibration curves (Figure 20 data) are plotted as lines, while results from the constant and stepped interference experiments are indicated as circle and crosses, respectively. The error bar for the data points are smaller than the symbols used in the plot. The various calibration results are practically coincident, indicating no practical cross-interference between CO_2 and CO.

The performance of the sensor as it has be discussed so far was published by myself and co-authors in a paper of the journal Applied Spectroscopy [14]. However, since this publication the performance of the LEDs has been increased by reevaluating the driving electronics as was discussed in chapter 3. For the reevaluation, Alicat mass flow controllers (MC series 10SCCM and 50SCCM) which contained some noise concentrations at low concentrations. With these enhancements the CO_2 detectivity limit was improved to 8ppm and the CO detectivity limit was improved to 300ppm, a 73.3% and 25% reduction respectfully.

Time Resolutions

The analysis procedure provides for 1kHz (1-ms) measurement rate. For each measurement, the detector signal was recorded at 10^6 Hz for one second to obtain 10^6 samples.

The data was split in to 1000 time bins each containing 1000 data points, and a Fast Fourier Transform (FFT) was performed on each bin in order to determine the signals (irradiance surrogate) from the three LEDs. After normalizing the two measurement LED signals using the reference LED signal, the absorbance values were calculated per Eq.1, but including a factor to account for differing optical losses between the various LED sources; i.e., the absorbance was calculated as $-\ln\left(\frac{I_{4.2}}{I_{3.6}}c_{\mathrm{CO_2}}\right)$ for CO_2 and $-\ln\left(\frac{I_{4.7}}{I_{3.6}}c_{\mathrm{CO}}\right)$ for CO, where $c_{\mathrm{CO_2}}$ and c_{CO} are the loss factors determined from measurement of a non-absorbing N_2 sample. This analysis procedure provided for simultaneous CO_2 and CO measurements at 10^3 Hz. For the steady state measurements, the standard deviation between the 1000 bins was used to quantify measurement uncertainty. Because the analysis procedure provides for 10^3 Hz measurement rate, the sensor is theoretically able to record fluctuations in absorbance of up to 500Hz (the Nyquist frequency) without aliasing, and practically able to accurately resolve transients of up to 250Hz. This temporal resolution is sufficient for engine-development and -research applications. The temporal resolution could be further improved by improving the LED throughput (and signal-to-noise ratio) as discussed above and faster signal acquisition, thus enabling use of shorter analysis bins.

The intrinsic sensor speed, independent of gas dynamics associated with the measurement cell, was characterized via temporal-resolution measurements, and demonstrated the fastest transients the sensor can resolve. Although gas dynamics will certainly limit temporal resolution of the sensor configuration using the measurements cell (cf. Figure 18), the intrinsic sensor speed is relevant to direct sensor applications; e.g., where the measurement cell is replaced by an engine intake runner for line-of-sight measurements. Moreover, the intrinsic temporal resolution

establishes a baseline performance standard that can be references to assess sensor improvements. For these experiments, the combined-LEDs beam was modulated from 25 to 400Hz using a 10-window optical chopper with various layers of polymer (polypropylene office material, Scotch tape, etc.) placed over three of the ten windows as shown in Figure 23. As the chopper rotates, it effectively turns the LED beam on and off via the open and solid portions of the wheel, respectively, and the polymer-covered windows simulate absorption; it is known that the polymer has broad absorption features around the 3.6μm Reference LED emission region. Of course the intrinsic sensor response is independent of the specific LED used for the assessment, and so the same response would be measured if real or synthetic absorption occurred at the CO_2 or CO wavelengths.

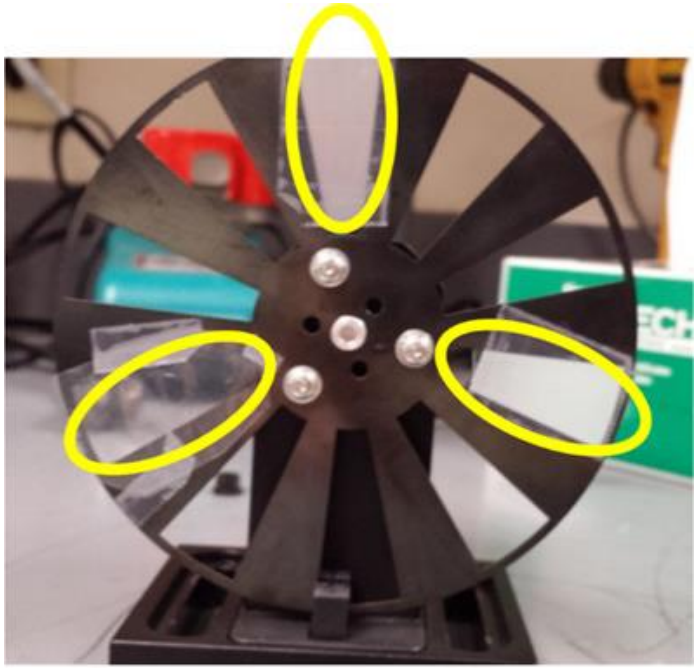

Figure 23: Optical chopper used for beam modulation in the temporal response studies, with three windows covered with various layers of polymer sheet to simulate absorption (highlighted in yellow).

Figure 24 shows results of the temporal response measurements to indicate resolution sufficient for intra-cycle-resolved engine measurements. The high-signal peaks are associated with the seven open chopper-wheel windows in Figure 23, the zero-signal points are associated with the ten solid windows, and the intermittent-signal peaks with the three polymer-covered windows which synthesized absorption. The magnitude of the intermediate peaks reflects the number of polymer layers covering each chopper window, with lower signal level indicating greater number of absorbing layers. The clear 2-3-2 temporal pattern of the high-signal peaks reflects the spatial geometry of Figure 23, and can be used to assign the intermediate peaks to specific windows. Specifically, the intermediate peaks surrounding the three high-signal peaks are the two lower circled windows in Figure 23 surrounding the three open chopper windows. Moreover, these two intermediate peaks have the greatest (ca. 1a.u.) and least (ca. 0.35a.u.) intermediate signal level, indicating the least and greatest number of absorbing polymer layers, respectively. Correspondingly, the middle (ca. 0.6a.u.) intermediate signal corresponded to the chopper window opposite the three open windows, and had the intermediate number of absorbing polymer layers. This logical interpretation of the Figure 24 patterns was consistent with the actual configuration of the chopper (i.e., number and distribution of absorbing layers), and is evidence of the sensor's temporal resolution beyond the ability to resolve individual chopper-window events. At 250Hz modulation, a chopper window should pass the LED beam every 4ms, which is consistent with the results shown in Figure 24a. This corresponds to 24 crank-angle-degrees (CAD) for an engine operating at 1000RPM, and indicates the ability to resolve transients on the order of individual (intake or exhaust) valve events. While the experiments performed do not account for sources of interference that may be present in actual engine measurements, the results illustrate that the sensor

has sufficient temporal resolution for resolving cylinder-to-cylinder and cycle-to-cycle variations in intake charge and combustion completion; combustion uniformity can be accessed via intake-manifold measurements, and combustion-completion fluctuations could be assessed via CO-CO_2 ratio variations [13].

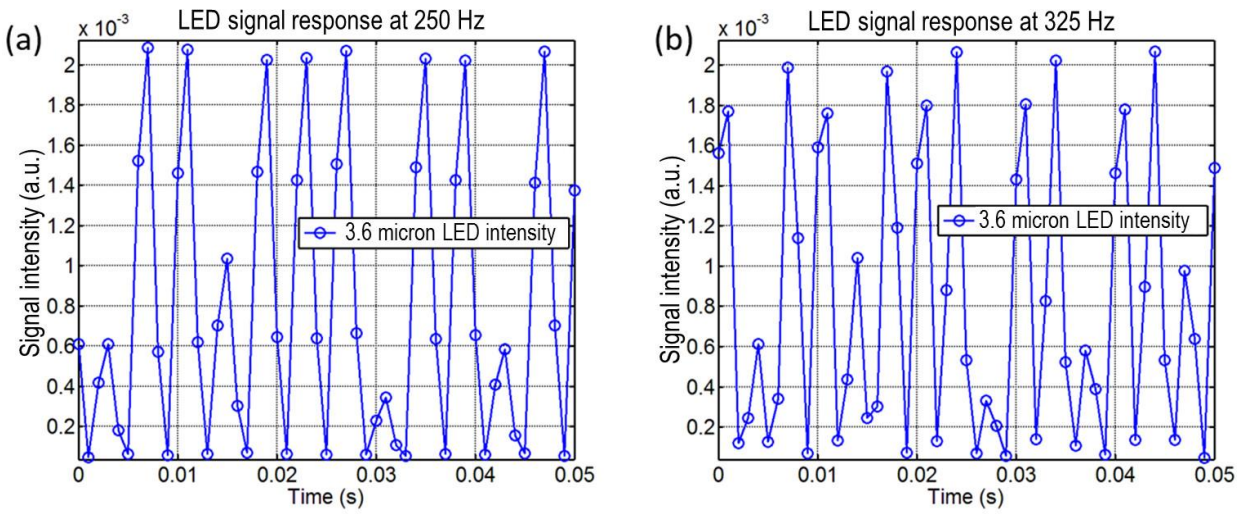

Figure 24: Temporal-resolution measurement results for LED modulation at (a) 250Hz and (b) 325Hz.

Faster transients could be resolved with alternate analysis bin size or higher DAQ speed. The 250Hz modulation results in Figure 24a indicate measurements below the Nyquist limit and synchronous with the measurement rate; in this synchronous case, there are exactly 4 measurements per modulation cycle resulting in consistent signals for the various open-window peaks. Figure 24b demonstrates the nature of transitioning beyond faithful transient characterization. Although 325Hz modulation is below the Nyquist limit and the results clearly show the patterns of the open and synthetic-absorption windows, the transients show more temporal variations compared to the 250Hz results. This is due to the nonsynchronous analysis

and modulation; specifically, at 325Hz, there are ca. 3.08 measurements per modulation cycle, causing the measurements to progressively walk through the modulations. This is manifested by the varying peak heights through the chopper revolution. For instance, the open-window high-signal-level peaks vary in magnitude because different points around the modulation peaks are sampled in this nonsynchronous mode. Similarly, there are differences in transient shape for identical transients in subsequent chopper modulations; e.g., the high-peak pair around 0.009s and 0.042s in Figure 24b corresponds to the same chopper window, as does the intermediate peak at ca. 0.013s and 0.048s. This demonstrates the onset transient-response error, and such transient distortion would continue with increasing modulation rate until it was completely unresolved at the Nyquist limit. While the sensor has been demonstrated as having sufficient temporal resolution for engine-research applications, the temporal resolution could be further extended by increasing the measurement rate. This could be implemented by increasing the DAQ rate or modifying the analysis procedure to use smaller temporal analysis bins; e.g., the temporal resolution could be doubled to 2kHz by using 500 rather than 1000 data points per FFT analysis bin. Although the signal, noise and other practical tradeoffs would have to be considered, this provides a general framework for further extending the sensor temporal resolution.

Environmental Chamber Evaluations

The environmental chamber shown in Figure 19 was used in evaluating the sensor's performance at near space like conditions. The intent of this experiment is to prepare the sensor for a high altitude balloon flight in September where it will reach an altitude of up to 35km where it can see conditions of -40°C and 1/100atm (7.6Torr). The environmental chamber was able to reach a pressure around 2Torr and a temperature of about -15°C. The primary concern is proper

thermal control of critical components at low pressure which the chamber is successfully able to replicate. The first run in the chamber we just ran the sensor to confirm everything operated as expected. This was also the first time the TECs were to be used in reverse. The test ran for an hour with success. The LEDs and detector thermal management plan were very successful.

We also ran a test without cooling the chamber (ambient temperature, low pressure) and found that the driver modules had trouble maintaining their temperature, however. At the moment their temperature is maintained passively with heatsinks however more active means may be necessary in the future. Alternatively, or perhaps more preferable, they may be replaced with more efficient drivers that produce much less heat. This is not a critical issue at the moment as there are no immediate plans at running the sensor in these conditions.

CHAPTER 5: CONCLUSIONS AND FUTURE WORK

Conclusions

A sensor for simultaneous detection of CO and CO_2 was developed using low-cost LEDs. The sensor was able to detect concentration changes as small as 8ppm and 300ppm for CO_2 and CO, respectively; with no cross-interference between CO_2 and CO. Temporal-response measurements indicated that the sensor can resolve fast transients of up to 250Hz, which is sufficient to resolve cylinder-to-cylinder and cycle-to-cycle variations in an engine operating at 1000RPM, assuming the sensor's implementation effectively mitigates interferences from operating in an actual engine environment. This sensor provides the potential to be implemented for on-board monitoring, diagnostics and control of performance fluctuations associated with these CO and CO_2, including EGR, and combustion completion and stability. The method and design developed here is applicable to developing sensors for a variety of gases, as a number of important gases, such as NO_2, N_2O, and CH_4, have fundamental absorption bands in the MIR spectral region.

Several insights were gained regarding increasing the sensors detection limit, sensitivity and temporal resolution. The CO_2 sensitivity was up to 10-times greater than CO because a greater number of CO_2 absorption features were measured by the broadband measurement. However, the CO_2 sensitivity degraded much faster than CO (although CO_2 sensitivity remained greater throughout) at higher concentrations because the stronger CO_2 absorption transitions entered saturation before the weaker CO transitions. The CO sensitivity and detection limit could be improved without compromising the cross-interference performance by using a broader LED bandpass filter that incorporated the longer-wavelength CO_2 absorption transitions (in the ca. 4.7-5um region) clipped by the current filter. Temporal resolution could be further improved by using

higher DAQ speeds and/or reducing the FFT analysis bin size; this could be further enabled by increasing the sensor SNR by increasing LED emission throughput via improved optical design. Nevertheless, the LED sensor has demonstrated performance for advancing engine and combustion research in its existing state, and these insights provide a pathway for further expanding the range of applicability.

The current detectivity limit for CO and CO_2 still has a lot of room for improvement from the ~80% optical signal loss and to reduction electrical noise. The use of beam splitters has significant consequences to signal loss, other forms of beam multiplexing should be considered suck as tightly spaced arrays. Reducing optical losses due to the LEDs incoherent nature will tricky, most of these losses are at the detector face which as 1x1mm. A larger detector face generally reduces detectivity and makes it more sensitive to noise. Currently the circuits experience some faint cross-over noise from the other LEDs signals. The circuit is also powered by batteries which are not well regulated and so, as their voltage drops off, the LEDs magnitude reduces. Finally, for test at UCF we used Alicat mass flow controllers which experience have a lot of low end noise. These issues carry over into the sensors sensitivity.

In addition to the lab-based sensitivity, detection limit, noise and cross interference addressed here, engine applications require additional considerations including, background IR interference, interference from other combustion products such as nitrous oxide (N_2O), and vibration-induced noise. The frequency based analysis procedure would aid in rejecting some interference and noise sources possible in actual engine experiments, as signals at frequencies other than those specified for the LED modulation are be rejected. Thermal emissions from a hot

engine surface would most likely be at too low of a frequency to affect the measured signal; such thermal IR background would primarily be relevant in a probe-based sensor configuration [13]. Another approach that has been used to address background interference is to directly measure that background by momentarily turning off the LEDs and implementing an offset correction. Figure 2 shows that N_2O has absorption features of comparable magnitude to and overlapping those of CO and CO_2, and is thus a source of potential interference. Nitrous oxide emissions are practically negligible in IC engine exhaust compared to the percent levels of CO and CO_2, although N_2O can be produced in catalytic exhaust treatment devices. Nevertheless, potential cross-interference due to absorption from N_2O and other combustion products may be mitigated by using a narrower bandpass filter centered over the 4.8μm band of the CO absorption. Vibrations should not impact the performance of a well-designed and mechanically stable diagnostic based on extractive sampling, such as that of the current sensor, e.g. Figure 18. In separate work using a similar sensor designed to measure CO_2, it has been observed that the vibration of hollow-waveguides used for probe-based on-engine measurements increased the uncertainty in measurements from 0.1% in vibration-free laboratory calibrations to 1.1%; however, these uncertainties were much less than the actual CO_2 concentration fluctuations and did not limit practical application of the diagnostic [13]. We expect that vibrations would impact a probe-based configuration of the current sensor's performance similarly.

Future Work

Current development of the sensor is in adaptions for space vehicles and any environments that may be encountered during space flight. A high altitude balloon flight has been secured which will allow evaluation of the sensor at altitudes of 35km (-40°C, 1/100atm).

Additional flights are planned to follow and may also include parabolic flights or missions to the International Space Station (ISS). The goal is to develop the hardware so that it is rugged and a viable technology for a variety of sensor applications in a variety of environments. It is therefore crucial that the hardware can reject heat at low pressures, survive low temperature operation, have low drift (stable output), remain low power, and be insensitive to humidity. As the hardware is further refined it should become more compact with more efficient multiplexing approaches. This may take the form of tightly spaced arrays of LEDs which use custom integrated lenses. The driving electronics will also need to be refined to a more efficient design as the current system produce excessive waste heat.

APPENDIX I: SPECIFICATION SHEETS FOR CRITICAL COMPONENTS

LED36TO8TEC Specifications (3.6μm cooled LED)

Optically Immersed 3.6 µm LED in heat-sink optimized housing			LED36Sr
Peak wavelength	λ_{max}	µm	3.65±0.05
Pulsed power at I=1 A	P_{pulsed}	µW	350±70
CW power at I=200 mA	P_{CW}	µW	135±25
Switching time	τ	ns	≤20

Code	Thread	Emission size, mm	Lens material	Far-field pattern FWHM, deg.	Optical axis deviation, deg	Operation (storage) conditions, ºC
LED36Sr	M5×0.5	Ø 3.3	Si	≤20	≤7	-25÷+60 (+80)
LED36TO8TEC			Si lens and quartz window			

Product view

LED36Sr

LED36TO8TEC

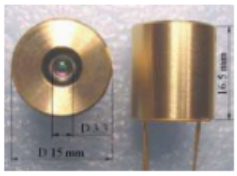

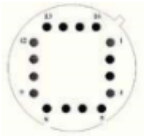

1 TEC –; 4 TEC +
8 LED +; 13 LED –
10, 11 thermosensor

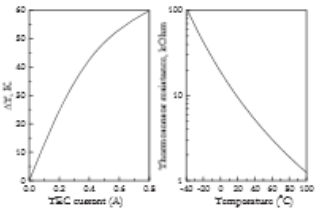

- ✓ All devices are stressed at 80°C (I=0) and I=200 mA (CW, 20°C) for 10 hrs before final test and shipping to a customer.
- ✓ Beam divergence of the LEDs is small and thus we recommend adjusting LED position regarding to the detector system before final evaluation/use of the devices.
- ✓ All data are valid for room temperature (22°C) and LED attached to a heatsink. Heatsink is important for normal LED operation especially in the CW mode.
- ✓ Polarity: see Product view. In near future two color wires will be used.

Output power vs. current, current-voltage curve and emission spectra

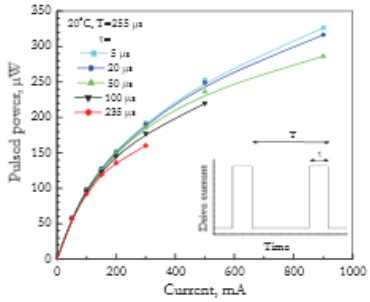

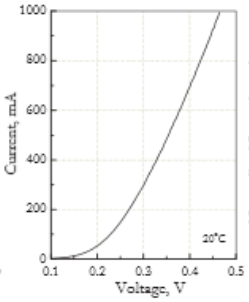

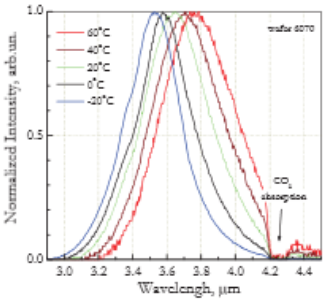

Output power and peak wavelength vs. temperature, far-field pattern and maximal current vs. operation conditions

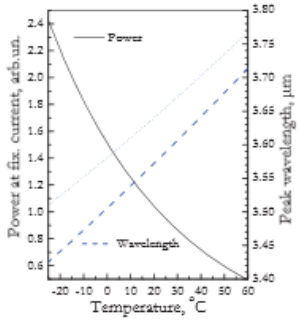

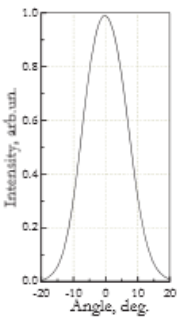

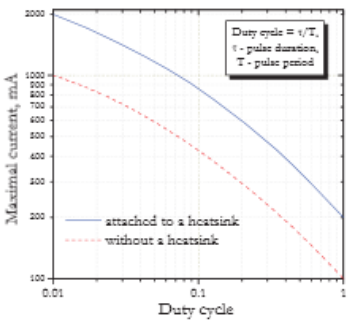

Updated 28.04.09

LED42TO8TEC Specifications (4.2μm cooled LED)

Optically Immersed 4.2 µm LED in heat-sink optimized housing			LED42Sr
Peak wavelength	λ_{max}	µm	4.2±0.1
Pulsed power at I=1 A	P_{pulsed}	µW	70±15
CW power at I=200 mA	P_{CW}	µW	25±5
Switching time	τ	ns	≤20

Code	Thread	Emission size, mm	Lens material	Far-field pattern FWHM, deg.	Optical axis deviation, deg	Operation (storage) conditions, °C
LED42Sr	M5×0.5	Ø 3.3	Si	≤20	≤7	-25÷+60 (+80)
LED42TO8TEC			Si lens and quartz window			

Product view

LED42Sr

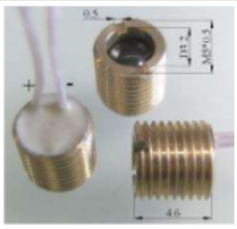

LED42TO8TEC

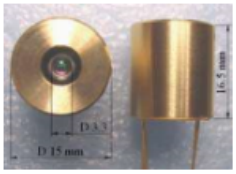

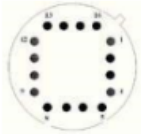

1 TEC –; 4 TEC +
8 LED +; 13 LED –
10, 11 thermosensor

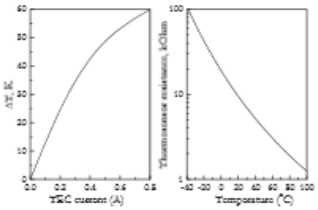

- ✓ All devices are stressed at 80°C (I=0) and I=200 mA (CW, 20°C) for 10 hrs before final test and shipping to a customer.
- ✓ Beam divergence of the LEDs is small and thus we recommend adjusting LED position regarding to the detector system before final evaluation/use of the devices.
- ✓ All data are valid for room temperature (22°C) and LED attached to a heatsink. Heatsink is important for normal LED operation especially in the CW mode.
- ✓ Polarity: see Product view. In near future two color wires will be used.

Output power vs. current, current-voltage curve and emission spectra

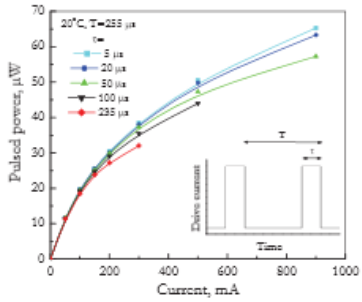

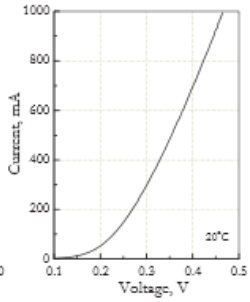

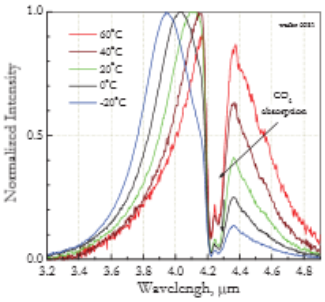

Output power and peak wavelength vs. temperature, far-field pattern and maximal current vs. operation conditions

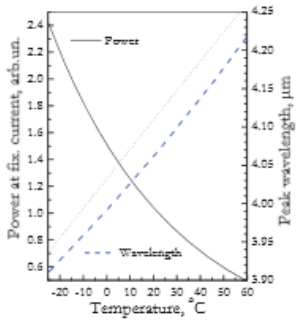

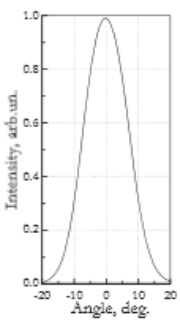

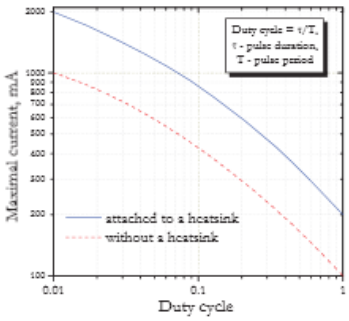

Updated 28.04.09

LED47TO8TEC Specifications (4.7μm cooled LED)

Optically Immersed 4.7 µm LED in heat-sink optimized housing			LED47Sr
Peak wavelength	λ_{max}	µm	4.7±0.05
Pulsed power at I=1 A	P_{pulsed}	µW	25±5
CW power at I=200 mA	P_{CW}	µW	5±1
Switching time	τ	ns	≤20

Code	Thread	Emission size, mm	Lens material	Far-field pattern FWHM, deg.	Optical axis deviation, deg	Operation (storage) conditions, ºC
LED47Sr	M5×0.5	Ø 3.3	Si	≤20	≤7	-25÷+60 (+80)
LED47TO8TEC			Si lens and sapphire window			

Product view

LED47Sr

LED47TO8TEC

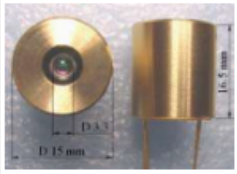

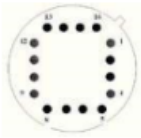

1 TEC –; 4 TEC +
8 LED +; 13 LED –
10, 11 thermosensor

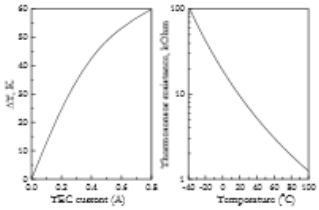

- ✓ All devices are stressed at 80°C (I=0) and I=150 mA (CW, 20°C) for 10 hrs before final test and shipping to a customer.
- ✓ Beam divergence of the LEDs is small and thus we recommend adjusting LED position regarding to the detector system before final evaluation/use of the devices.
- ✓ All data are valid for room temperature (22°C) and LED attached to a heatsink. Heatsink is important for normal LED operation especially in the CW mode.
- ✓ Polarity: see Product view. In near future two color wires will be used.

Output power vs. current, current-voltage curve and emission spectra

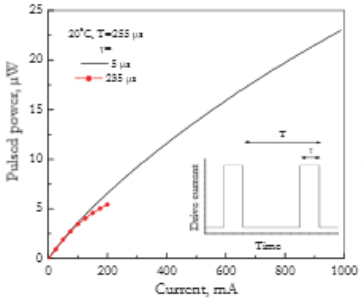

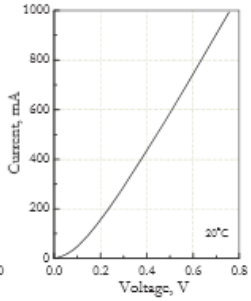

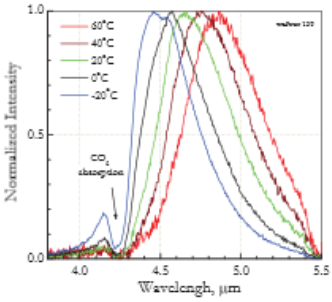

Output power and peak wavelength vs. temperature, far-field pattern and maximal current vs. operation conditions

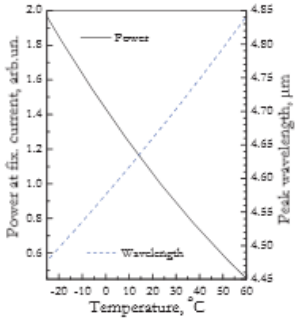

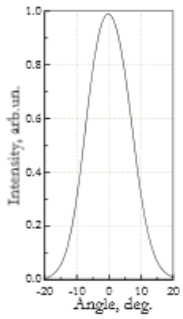

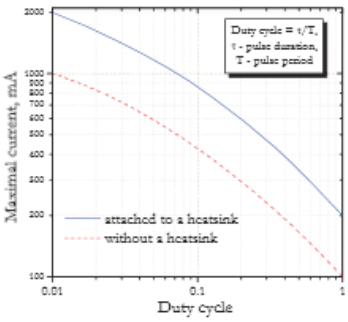

Updated 28.04.09

PVI-3TE Photovoltaic Detector Specifications

PVI-3TE SERIES

2-12 µm IR PHOTOVOLTAIC DETECTORS THERMOELECTRICALLY COOLED OPTICALLY IMMERSED

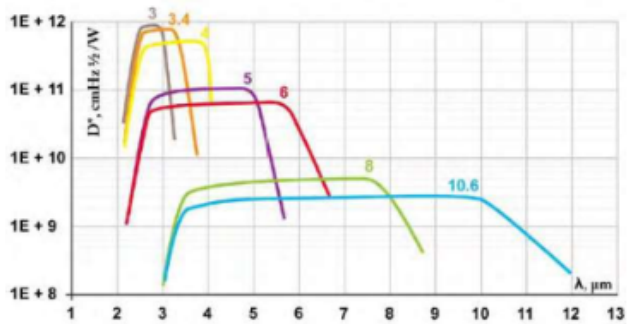

FEATURES

- High performance in the 2-12 µm wavelength range
- Fast response
- No flicker noise
- Convenient to use
- Wide dynamic range
- Compact, rugged and reliable
- Low cost
- Prompt delivery
- Custom design upon request

DESCRIPTION

PVI-3TE-λ_{opt} photodetectors series (λ_{opt} - optimal wavelength in micrometers) feature 3-stage thermoelectric cooler IR photovoltaic detector, optically immersed to high refractive index GaAs hyperhemispherical (standard) or hemispherical or any intermediate lens for different acceptance angle and saturation level. The devices are optimized for the maximum performance at λ_{opt}. Cut-on wavelength can be optimized upon request. Reverse bias may significantly increase speed of response and dynamic range. It results also in improved performance at high frequencies, but 1/f noise that appears in biased devices may reduce performance at low frequencies. Highest performance and stability are achieved by application of variable gap (HgCd)Te semiconductor, optimized doping. Standard detectors are available in TO-8 packages with BaF2 windows. Other packages, windows and connectors are also available.

SPECIFICATION

@20°C

CHARACTERISTICS	UNITS	PVI-3TE-3	PVI-3TE-3.4	PVI-3TE-4	PVI-3TE-5	PVI-3TE-6	PVI-3TE-8	PVI-3TE-10.6
λ_{opt}	µm	3	3.4	4	5	6	8	10.6
Detectivity[1]:								
@ λ_{peak}	$cmHz^{1/2}/W$	$\geq 9\times10^{11}$	$\geq 7\times10^{11}$	$\geq 5\times10^{11}$	$\geq 1\times10^{11}$	$\geq 6\times10^{10}$	$\geq 5\times10^{9}$	$\geq 3\times10^{9}$
@ λ_{opt}		$\geq 7\times10^{11}$	$\geq 5\times10^{11}$	$\geq 3\times10^{11}$	$\geq 8\times10^{10}$	$\geq 3\times10^{10}$	$\geq 3\times10^{9}$	$\geq 1.5\times10^{9}$
Responsivity @ λ_{opt}	A/W	≥0.5	≥0.8	≥1	≥1.3	≥1.5	≥1	≥0.7
Time constant	ns	≤20	≤20	≤20	≤20	≤15	≤8	≤6
Resistance-optical area product	$\Omega\times cm^2$	≥24000	≥1500	≥600	≥30	≥2.5	≥0.04	≥0.02
Operating temperature	K	~210						
Acceptance angle, F/#	deg, -	36, 1.62						

[1] Data sheet states minimum guaranteed D* values for each detector model. Higher performance detectors can be provided upon request.

[2] Faster response may be achieved with high-frequency-optimized devices.

Type	Length or diameter [mm]									
	0.025	0.05	0.1	0.2	0.25	0.5	1	2	3	4
PVI-3TE-3					O	X	X	O		
PVI-3TE-3.4					O	X	X	O		
PVI-3TE-4					O	X	X	O		
PVI-3TE-5					O	X	X	O		
PVI-3TE-6					O	X	X	O		
PVI-3TE-8				X	X	X[1]	P			
PVI-3TE-10.6				X	X	X[1]	P			

[1] Custom detector may require reverse bias in order to increase dynamic resistance and improve frequency response.

X – standard detectors

P – default with reverse bias

O – detectors available on request, parameters may differ from these in data sheets

Warsaw Poland; e-mail: info@vigo.com.pl Agent: Boston Electronics, Brookline MA USA +1 617 566 3821; vigo@boselec.com

Wavelength Electronics WLD3343 General Purpose Driver

ELECTRICAL AND OPERATING SPECIFICATIONS

ABSOLUTE MAXIMUM RATINGS RATING	SYMBOL	VALUE	UNIT
Supply Voltage (Voltage on Pin 14)	V_{DD}	+4.5 to +12.5	Volts DC
Output Current (See SOA Chart)	I_{LD}	2.2 or 3	Amperes
Power Dissipation, $T_{AMBIENT}$ = +25˚C	P_{MAX}	9	Watts [1]
Operating Temperature, case [2]	T_{OPR}	- 40 to + 85 [3]	˚C
Storage Temperature	T_{STG}	- 65 to +150	˚C
Weight	WLD3343	0.6	oz

PARAMETER	TEST CONDITIONS	WLD3343-2A	WLD3343-3A	UNITS
OUTPUT				
Current, peak, see SOA chart		2.2	3	Amps
Compliance Voltage, Laser Diode Load	I_{LD} = 100 mA, 5 V	3.6		Volts
Compliance Voltage, Laser Diode Load	I_{LD} = 1.0 Amp, 5 V	3.5		Volts
Compliance Voltage, Laser Diode Load	I_{LD} = 2.0 Amps, 5 V	3.0		Volts
Compliance Voltage, Laser Diode Load	I_{LD} = 3.0 Amps, 5 V		3.0	Volts
Compliance Voltage, Laser Diode Load	I_{LD} = 100 mA,12 V	10.6		Volts
Compliance Voltage, Laser Diode Load	I_{LD} = 1.0 Amp,12 V	10.4		Volts
Compliance Voltage, Laser Diode Load	I_{LD} = 2.0 Amp,12 V	10.1		Volts
Compliance Voltage, Laser Diode Load	I_{LD} = 3.0 Amp,12 V		10.0	Volts
Rise Time	I_{LD}= Full Scale	460		nsec
Fall Time	I_{LD}= Full Scale	320		nsec
Bandwidth	Constant Current, Sine Wave	2.0		MHz
Bandwidth	Constant Power	(Depends on PD BW)		
Slow Start - Delay		0.24		Seconds
Slow Start - Ramp		0.01		Seconds
Leakage Current [4]		0		mA
CONSTANT CURRENT CONTROL				
Short Term Stability, 1 hour	$T_{AMBIENT}$ = 25˚C	200	200	ppm
CONSTANT POWER CONTROL				
Short Term Stability, 1 hour	$T_{AMBIENT}$ = 25˚C	0.01		%
Long Term Stability, 24 hours	$T_{AMBIENT}$ = 25˚C	0.05		%

Notes:

[1] In the WLD3343 and WLD3343-2L models, internal power dissipation is 1.2 W (without heatsink), 2 W (with heatsink), and 9 W (with heatsink and fan). In the WLD3343-3A and WLD3343-3L models, internal power dissipation is 2 W (without heatsink), 3 W (with heatsink), and 10 W (with heatsink and fan).

[2] With Revision D forward of the WLD3343, an internal thermostat has been added to activate Shutdown (SHD) when the internal temperature exceeds 105˚C. The output will be re-enabled after a 250 to 300 msec slow-start once the internal temperature drops below 95˚C.

[3] Max ambient operating temperature of the WLD3343-3A and WLD3343-3L is 45°C.

[4] Leakage current specification is based on full current set by R_{SENSE}. See page 9 for information on setting the current range. Minimum turn on current in the 200 mA range is 350 µA. Minimum turn on current in the 2 A range is 12 mA. This specification applies to Rev. E forward.

Noise: To further reduce noise, the WLD3343-2L and WLD3343-3L models are available. Both are about 2.5 times lower noise than the WLD3343 and WLD3343-3A, respectively. Constant Power (CP) mode is not available in these models.

APPENDIX II: DAQ CODE (VIS)

FPGA Main.vi

FPGA Main.vi is the only VI that runs on the FPGA. In consists of 5 whiles loops. Three for outputting LED signals, one for TEC and thermistor control, and one for the detector.

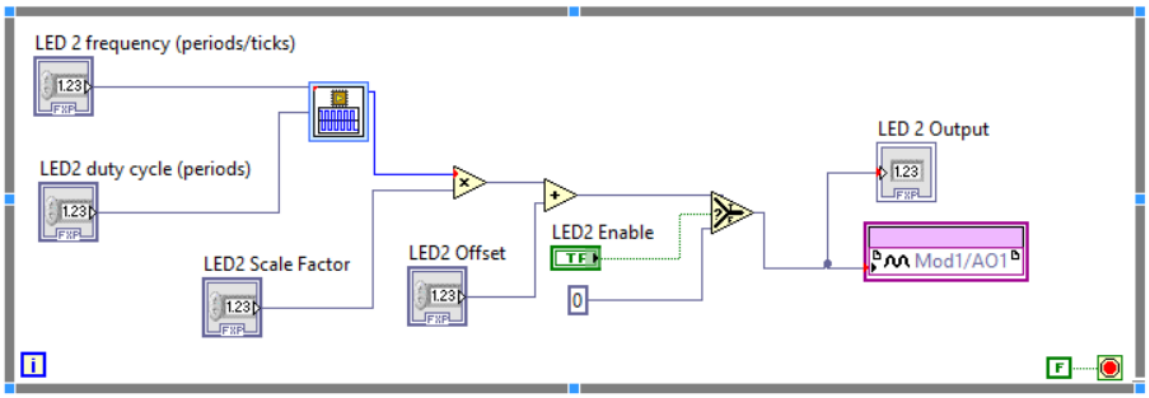

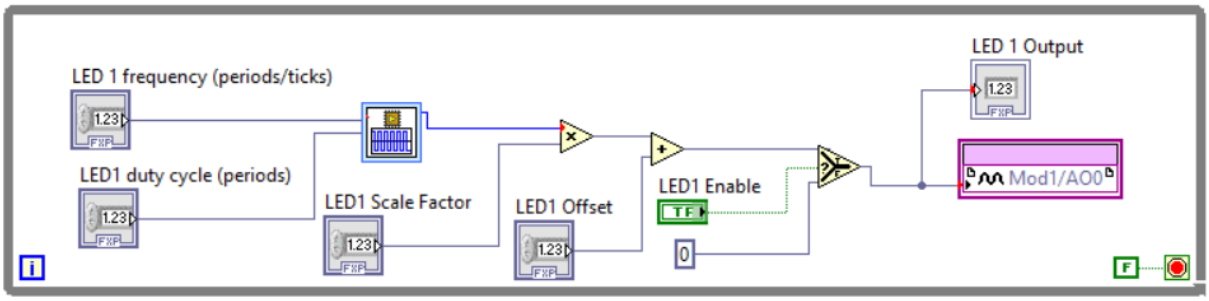

LED Signal Loop

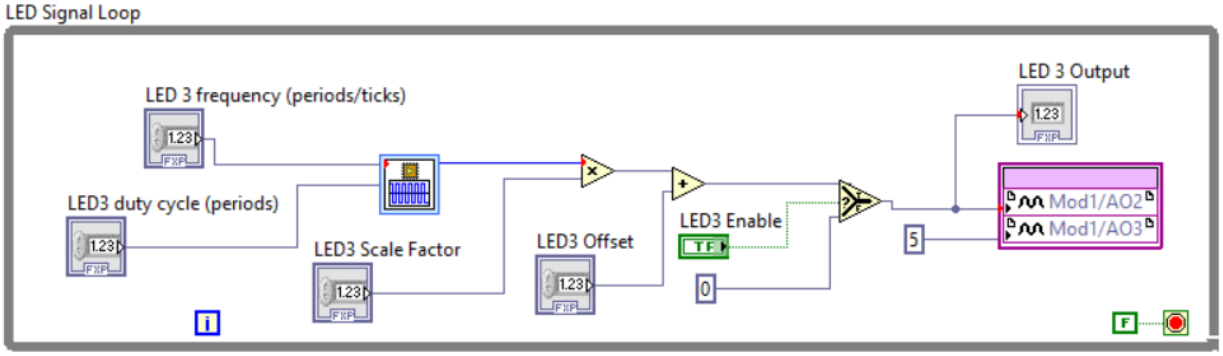

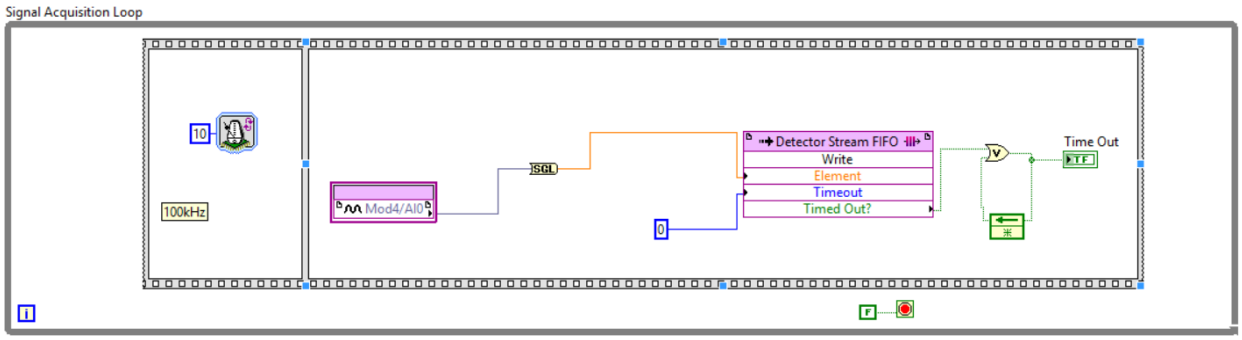

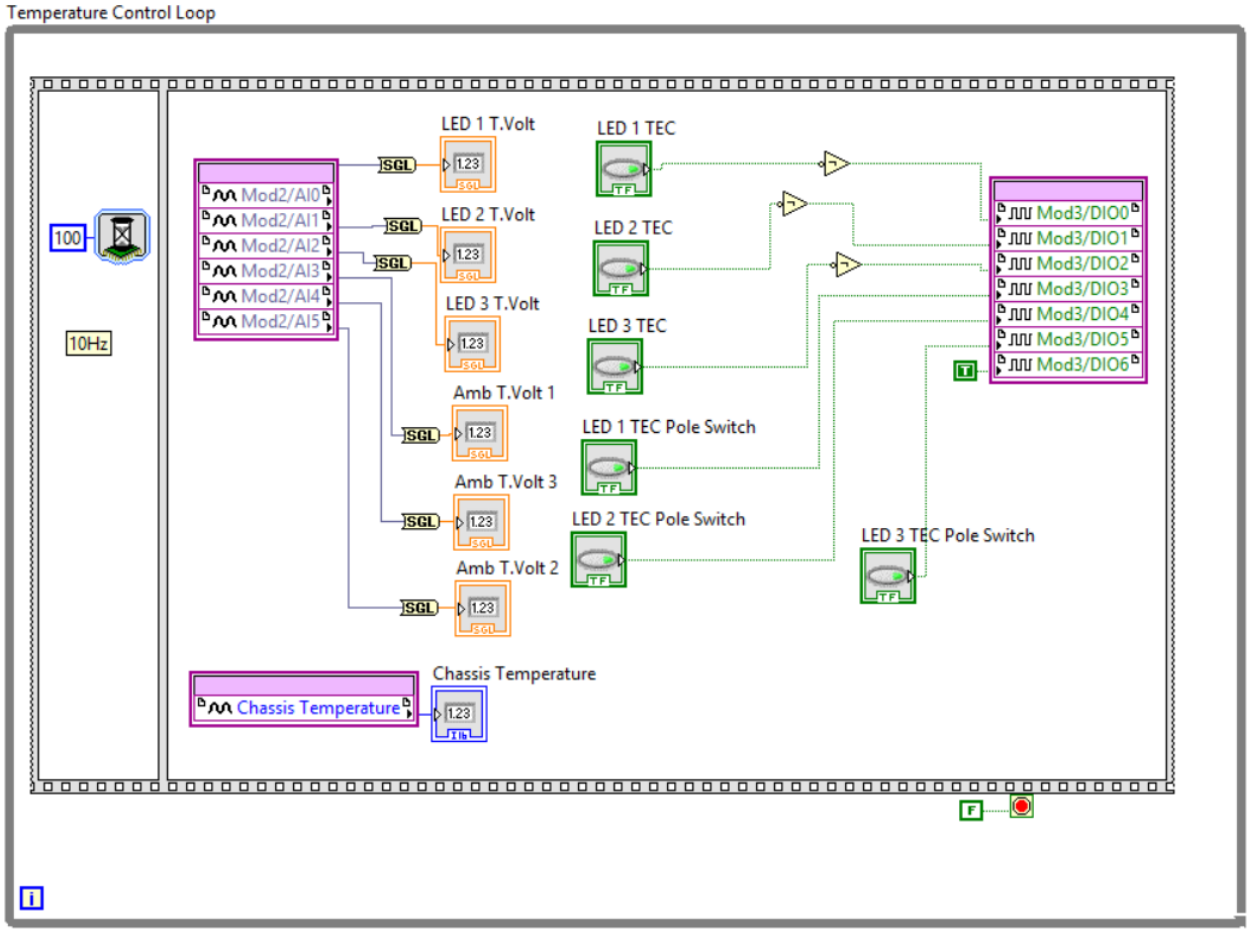

RT Main2.vi

This is the only VI that runs on the real-time host though it contains two subVIs. This has three loops, one for (LED) temperature control, one for data saving, and one for streaming and

buffering data. One subVI is just used to convert thermistor values to temperature (this VI is not shown). The other is used in the TEC pole switch decision logic.

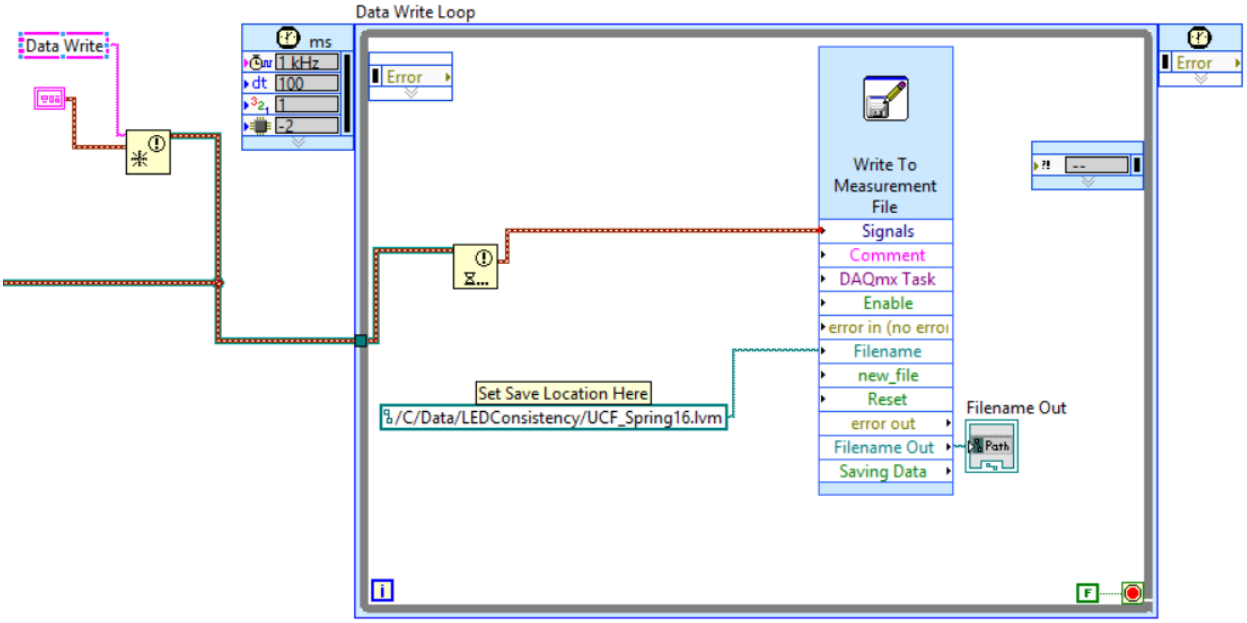

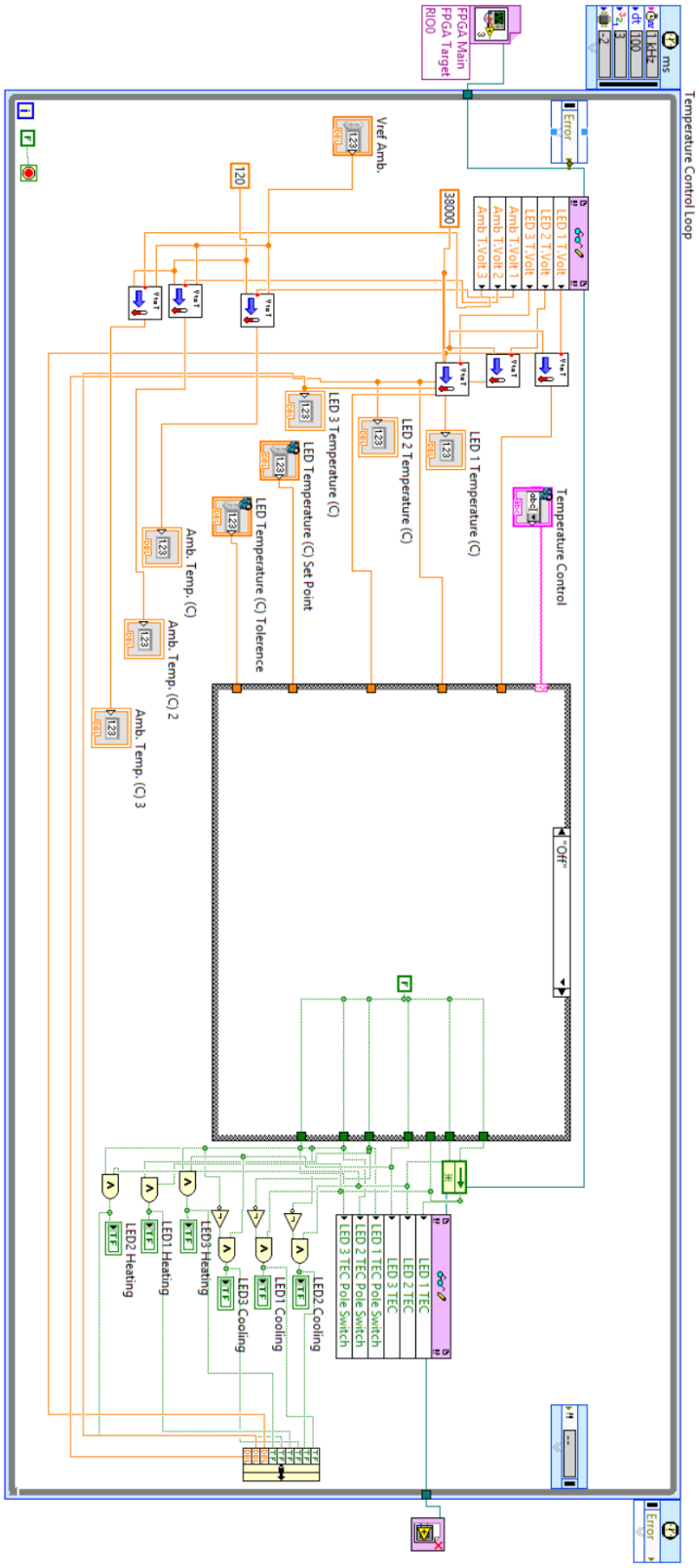
Temperature Control Loop
ms
1 kHz
100
FPGA Main
FPGA Target
RIO0
Error
LED 1 T.Volt
LED 2 T.Volt
LED 3 T.Volt
Amb T.Volt 1
Amb T.Volt 2
Amb T.Volt 3
38000
120
Vref Amb.
Temperature Control
LED 1 Temperature (C)
LED 2 Temperature (C)
LED 3 Temperature (C)
LED Temperature (C) Set Point
LED Temperature (C) Tolerence
Amb. Temp. (C)
Amb. Temp. (C) 2
Amb. Temp. (C) 3
"Off"
LED 1 TEC
LED 2 TEC
LED 3 TEC
LED 1 TEC Pole Switch
LED 2 TEC Pole Switch
LED 3 TEC Pole Switch
LED2 Cooling
LED1 Cooling
LED3 Cooling
LED3 Heating
LED1 Heating
LED2 Heating
Error

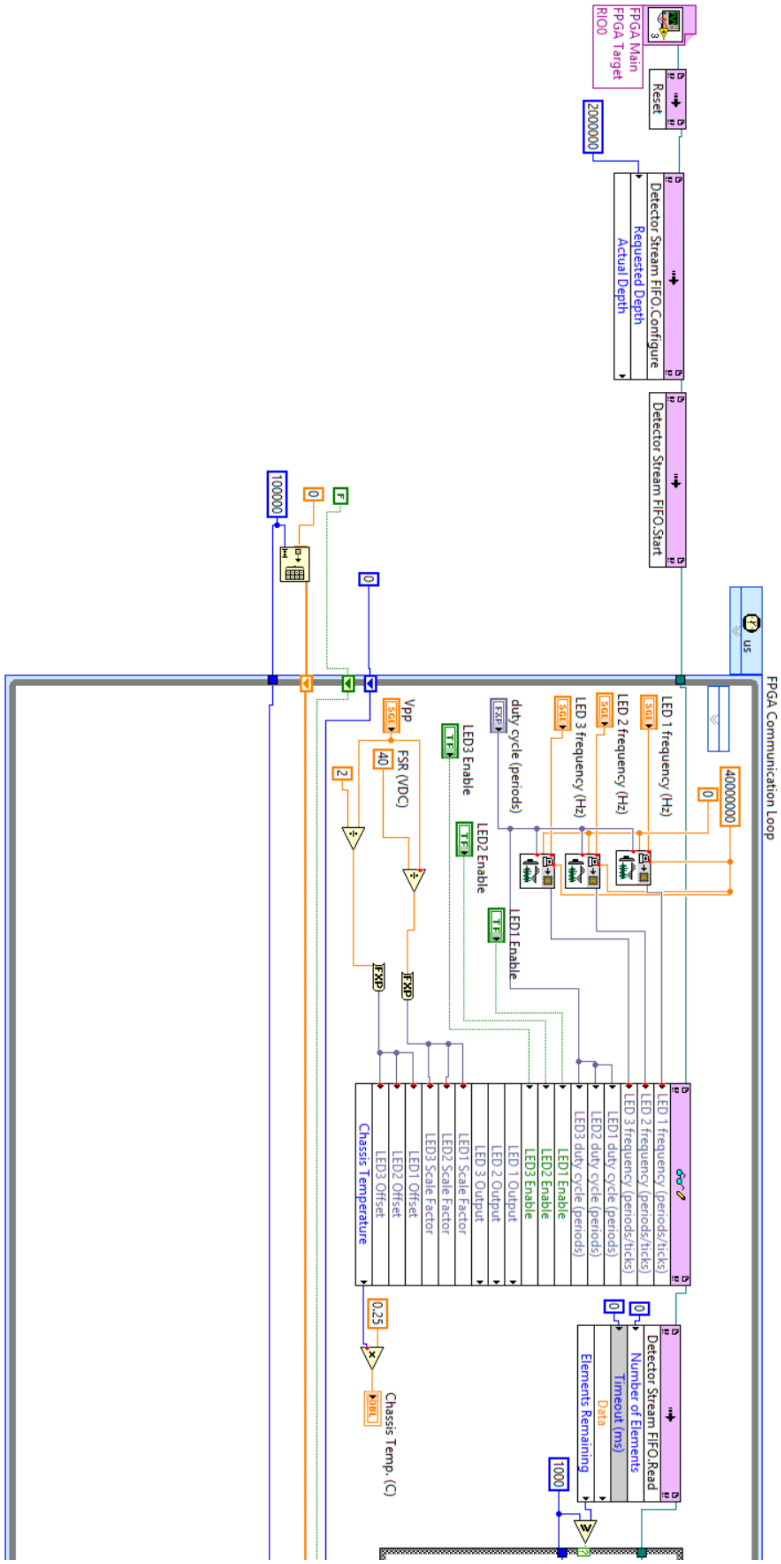
FPGA Communication Loop
Detector Stream FIFO.Configure
Requested Depth
Actual Depth
FPGA Main
FPGA Target
RIO0
Reset
2000000
Detector Stream FIFO.Start
4000000
LED 1 frequency (Hz)
LED 2 frequency (Hz)
LED 3 frequency (Hz)
duty cycle (periods)
LED3 Enable
LED2 Enable
LED1 Enable
Vpp
FSR (VDC)
40
2
LED 1 frequency (periods/ticks)
LED 2 frequency (periods/ticks)
LED 3 frequency (periods/ticks)
LED1 duty cycle (periods)
LED2 duty cycle (periods)
LED3 duty cycle (periods)
LED1 Enable
LED3 Enable
LED2 Enable
LED1 Output
LED 2 Output
LED 3 Output
LED1 Scale Factor
LED2 Scale Factor
LED3 Scale Factor
LED1 Offset
LED2 Offset
LED3 Offset
Chassis Temperature
Detector Stream FIFO.Read
Number of Elements
Timeout (ms)
Data
Elements Remaining
1000
0.25
Chassis Temp. (C)
100000

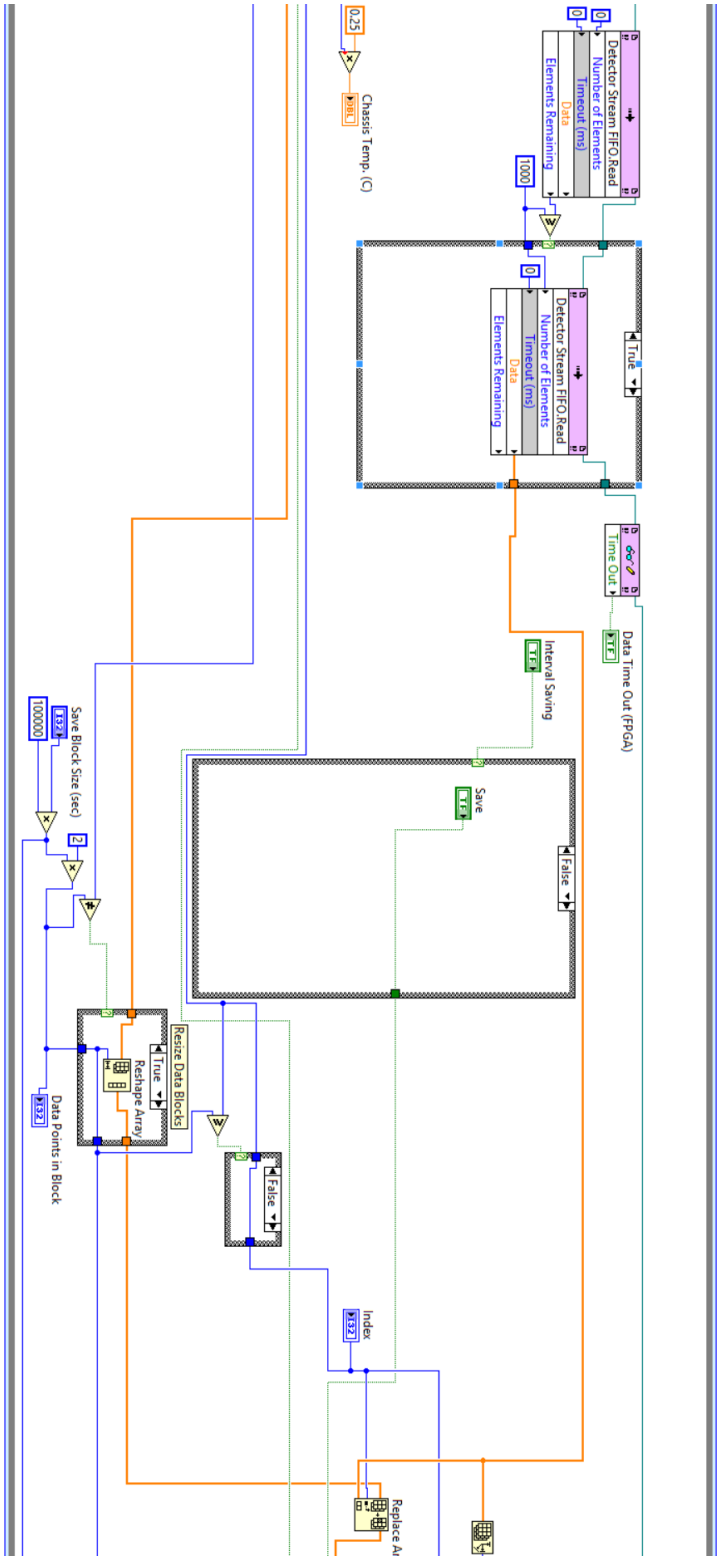
Detector Stream FIFO.Read
Number of Elements
Timeout (ms)
Data
Elements Remaining
0
1000
True
Time Out
Data Time Out (FPGA)
Interval Saving
Save
False
Chassis Temp. (C)
0.25
Save Block Size (sec)
2
100000
Resize Data Blocks
Reshape Array
Data Points in Block
Index
Replace Array

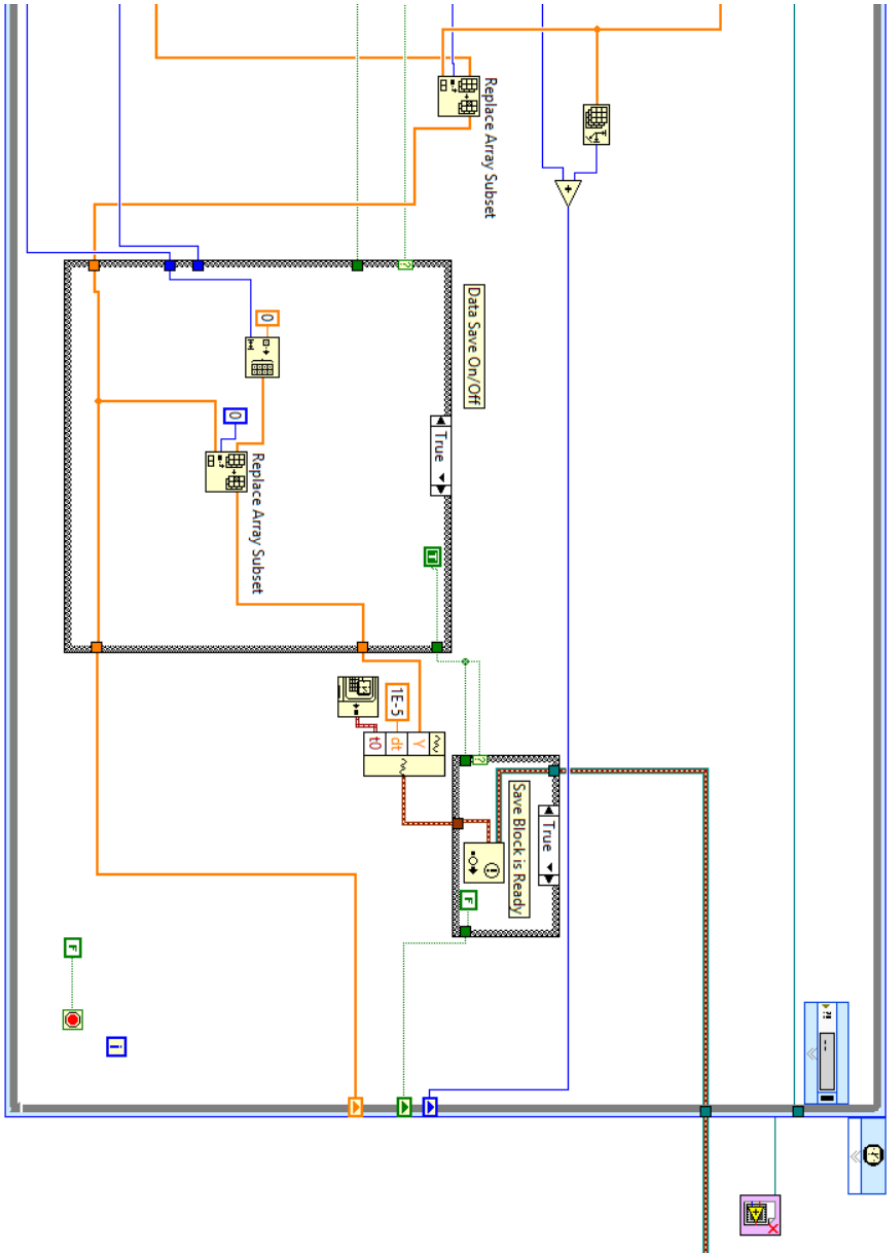
Replace Array Subset
Data Save On/Off
True
Replace Array Subset
0
0
1E-5
t0
dt
Y
Save Block is Ready
True

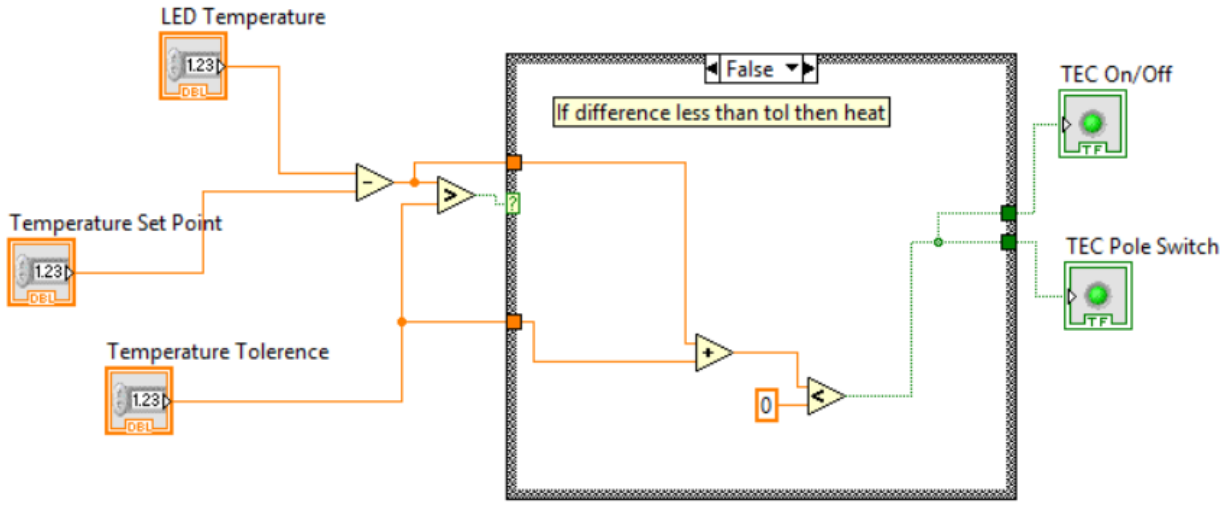

Lab Interface.vi

The lab interface is not a critical component and is only ran for diagnostics. When the sensor is ran headless (without a client) this VI does not run at all. Since the point of this VI is the user interface (UI) this is the only VI I am showing the UI. All controls are linked via shared variables. Since data in the interface isn't really time critical this is ok; it is simply meant as a check that everything is work as it should.

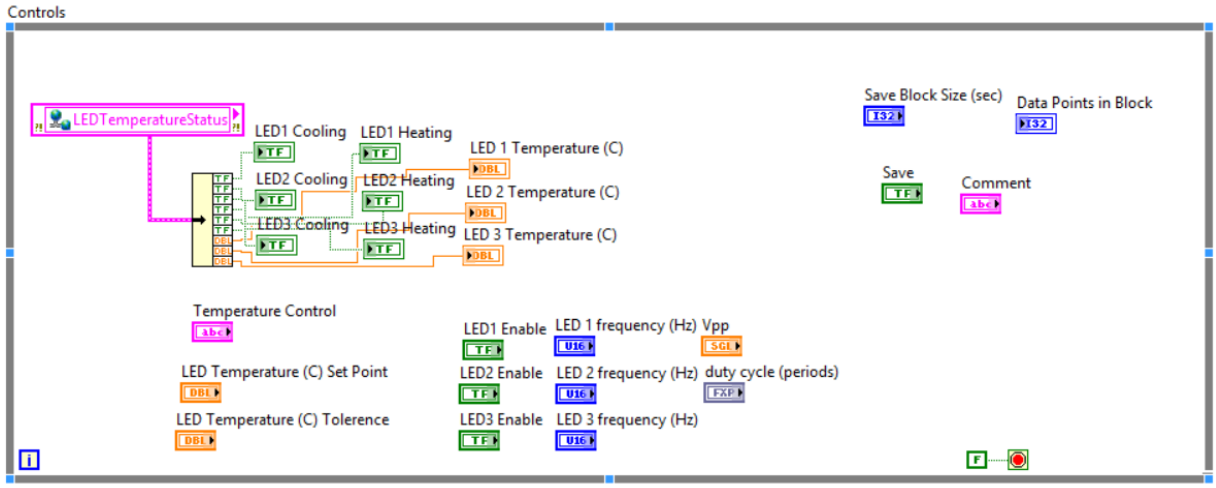

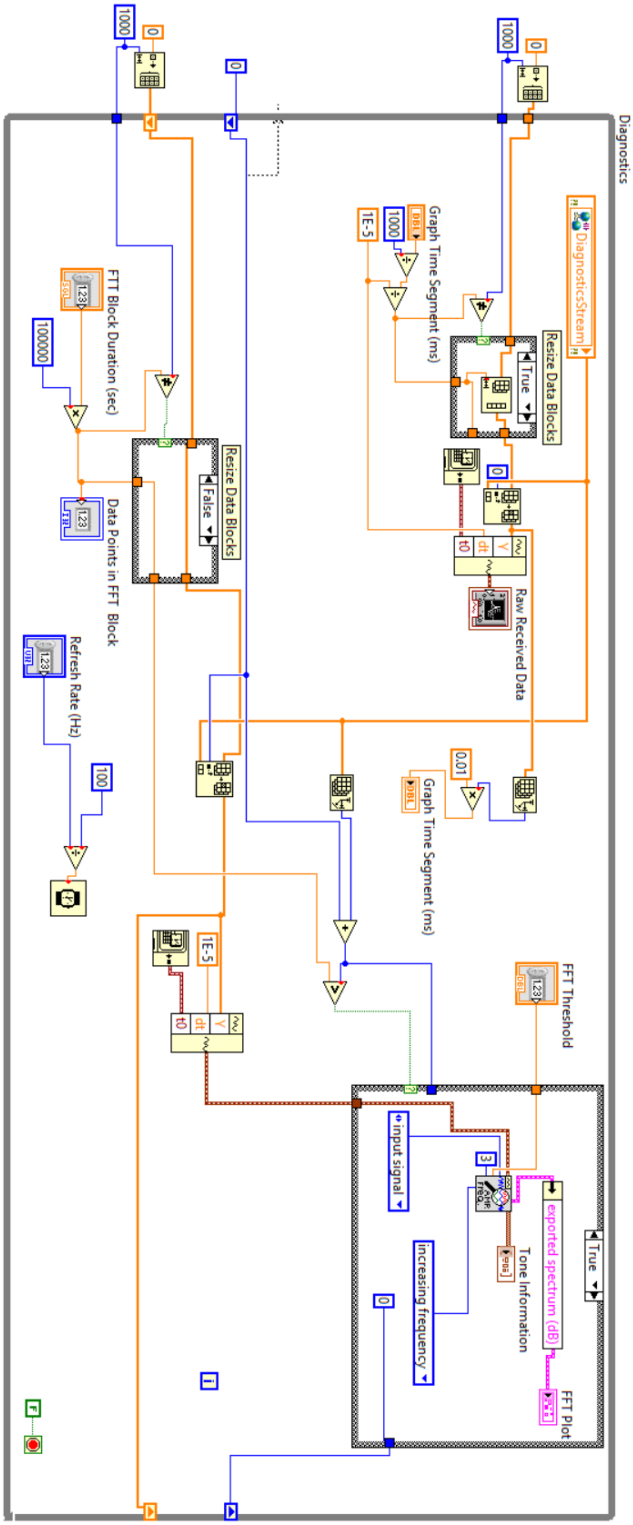
Diagnostics
DiagnosticsStream
Resize Data Blocks
True
Raw Received Data
Graph Time Segment (ms)
1000
1E-5
0.01
FFT Threshold
exported spectrum (dB)
Tone Information
FFT Plot
input signal
increasing frequency
3
Resize Data Blocks
False
FFT Block Duration (sec)
100000
Data Points in FFT Block
Refresh Rate (Hz)
100

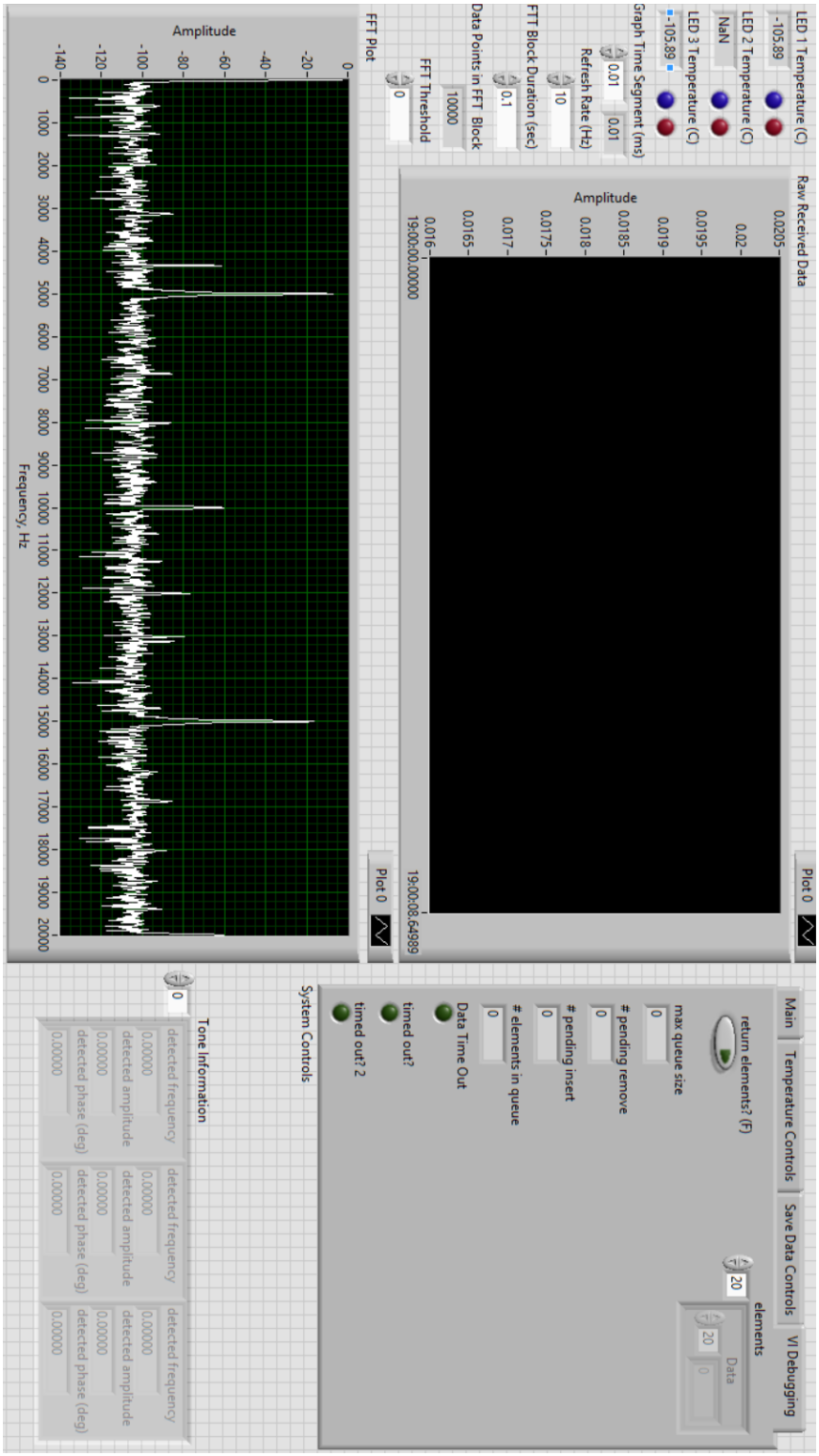
LED 1 Temperature (C)
-105.89
LED 2 Temperature (C)
NaN
LED 3 Temperature (C)
-105.89
Graph Time Segment (ms)
0.01
0.01
Refresh Rate (Hz)
10
FTT Block Duration (sec)
0.1
Data Points in FFT Block
10000
FFT Threshold
0
Raw Received Data
Amplitude
Plot 0
FFT Plot
Amplitude
Frequency, Hz
Main
Temperature Controls
Save Data Controls
VI Debugging
return elements? (F)
elements
max queue size
pending remove
pending insert
elements in queue
Data Time Out
timed out?
timed out? 2
System Controls
Tone Information
detected frequency
detected amplitude
detected phase (deg)

REFERENCES

[1] 2013, "International Energy Outlook 2013," D. o. Energy, ed.http://www.eia.gov/forecasts/ieo/pdf/0484(2013).pdf.

[2] Manley, D. K., McIlroy, A., and Taatjes, C. A., 2008, "Research needs for future internal combustion engines," Physics Today, 61, pp. 47-52.

[3] Alexander, L., Allen, S., Bindoff, N., Breon, F.-M., Church, J., Cubasch, U., Emori, S., Forster, P., Friedlingstein, P., Gillett, N., Gregory, J., Hartmann, D., Jansen, E., Kirtman, B., Knutti, R., Kanikicharla, K. K., Lemke, P., Marotzke, J., Masson-Delmotte, V., Meehl, G., Mokhov, I., Piao, S., Ramaswamy, V., Randall, D., Rhein, M., Rojas, M., Sabine, C., Shindell, D., Talley, L., Vaughan, D., and Xie, S.-P., 2013, "The IPCC Fifth Assessment Report Climate Change 2013," Intergovernmental Panel on Climate Change, http://www.climatechange2013.org/images/uploads/WGIAR5_WGI-12Doc2b_FinalDraft_All.pdf.

[4] Zheng, M., Reader, G. T., and Hawley, J. G., 2004, "Diesel engine exhaust gas recirculation––a review on advanced and novel concepts," Energy Conversion and Management, 45(6), pp. 883-900.

[5] Chandler, F., Ambrose, R., Biegel, B., Brown, T., Carter, J., Culbert, C., Edwards, C., Fox, J., Glaessgen, E., Hurlbert, K., Israel, D., Johnson, L., Kliss, M., Linne, D., Meador, M., Mercer, C., Meyer, M., Motil, B., Munk, M., Nesnas, I., Prince, J., Ryan, R., Scott, J., and Siochi, E., 2015, "2015 NASA Technology Roadmaps," NASA, ed.http://www.nasa.gov/offices/oct/home/roadmaps/index.html.

[6] Ren, W., Farooq, A., Davidson, D. F., and Hanson, R. K., 2012, "CO concentration and temperature sensor for combustion gases using quantum-cascade laser absorption near 4.7 μm," Applied Physics B, 107(3), pp. 849-860.

[7] Farooq, A., Jeffries, J., and Hanson, R. K., 2008, "CO2 concentration and temperature sensor for combustion gases using diode-laser absorption near 2.7 μm," Applied Physics B, 90(3-4), pp. 619-628.

[8] Teichert, H., Fernholz, T., and Ebert, V., 2003, "Simultaneous In Situ Measurement of CO, H2O, and Gas Temperatures in a Full-Sized Coal-Fired Power Plant by Near-Infrared Diode Lasers," Applied Optics, 42(12), pp. 2043-2051.

[9] Mihalcea, R. M., Baer, D. S., and Hanson, R. K., 1998, "Advanced diode laser absorption sensor for in situ combustion measurements of CO2, H2O, and gas temperature," Sumposium (International) on Combustion, 27(1), pp. 95–101.

[10] Schultz, I. A., Goldenstein, C. S., Jeffries, J. B., and Hanson, R. K., 2012, "TDL Absorption Sensor for In Situ Determination of Combustion Progress in Scramjet Ground Testing,"

Aerodynamic Measurement Technology, Ground Testing, and Flight Testing Conference, 28.

[11] Silver, J. A., 1992, "Frequency-modulation spectroscopy for trace species detection: theory and comparison among experimental methods," Applied Optics, 31(6), pp. 707-717.

[12] Rothman, L. S., Gordon, I. E., Babikov, Y., Barbe, A., Benner, D. C., Bernath, P. F., Birk, M., Bizzocchi, L., Boudon, V., Brown, L. R., Campargue, A., Chance, K., Cohen, E. A., Coudert, L. H., Devi, V. M., Drouin, B. J., Fayt, A., Flaud, J. M., Gamache, R. R., Harrison, J. J., Hartmann, J. M., Hill, C., Hodges, J. T., Jacquemart, D., Jolly, A., Lamouroux, J., Roy, R. J. L., Li, G., Long, D. A., Lyulin, O. M., Mackie, C. J., Massie, S. T., Mikhailenko, S., Müller, H. S. P., Naumenko, O. V., Nikitin, A. V., Orphal, J., Perevalov, V., Perrin, A., Polovtseva, E. R., Richard, C., Smith, M. A. H., Starikova, E., Sung, K., Tashkun, S., Tennyson, J., Toon, G. C., Tyuterev, V. G., Wagner, G., Müller, H., and Smith, M., 2013, "The HITRAN2012 molecular spectroscopic database," Journal of Quantitative Spectroscopy and Radiative Transfer.

[13] Yoo, J., Prikhodko, V., Parks, J. E., Perfetto, A., Geckler, S., and Partridge, W. P., 2015, "Fast Spatially-Resolved EGR Distribution Measurements in an Internal Combustion Engine using Absorption Spectroscopy," Applied Spectroscopy #(#), pp. #-#.

[14] Thurmond, K., Loparo, Z., Partridge, W. P., and Vasu, S., 2016, "A Light-Emitting Diode (LED) Based Absorption Sensor for Simultaneous Detection of Carbon Monoxide and Carbon Dioxide," Applied Spectroscopy.

[15] Puton, J., Jasek, K., Siodłowski, B., Knap, A., and Wiśniewski, K., 2002, "Optimisation of a pulsed IR source for NDIR gas analysers," Opto-Electronics Review, 10(2), pp. 97-103.

[16] Laine, D., Al-Jourani, M., Carpenter, S., and Sedgbeer, M., "Pulsed wideband IR thermal source," Proc. Optoelectronics, IEE Proceedings-, IET, pp. 315-322.

[17] Matveev, B. A., Gavrilov, G. A., Evstropov, V. V., Zotova, N. V., Karandashov, S. A., Sotnikova, G. Y., Stus, N. M., Talalakin, G. N., and Malinen, J., 1997, "Mid-infrared (3-5 μm) LEDs as sources for gas and liquid sensors," Sensors and Actuators B: Chemical, 39(1–3), pp. 339-343.

[18] Ioffe, I., 2013, "LEDs for the mid-infrared region of the spectrum (2-6 micrometers)," Ioffe Institute, http://www.ioffeled.com/index.php?option=com_content&view=article&id=52&Itemid=103.

[19] Perry, F., 2013, "IR Detectors from Vigo Systems," Bosten Electronics, http://www.boselec.com/products/documents/-VigoCatalog11-5-13WWW.pdf.

[20] 2013, "Zemax," Radiant Zemax, http://www.radiantzemax.com/en.

[21] Maukonen, D., Fredricksen, C. J., Muraviev, A. V., Alhasan, A., Calhoun, S., Zummo, G., Peale, R. E., and Colwell, J. E., "Planetary Atmospheres Minor Species Sensor (PAMSS)," Proc. SPIE Sensing Technology+ Applications, International Society for Optics and Photonics, pp. 91130N-91130N-91138.